Visible-Light Integrated Photonics for 3D-Printing and Trapped-Ion Systems

by

Sabrina M. Corsetti

B.S. Physics, University of Michigan – Ann Arbor (2021)

Submitted to the Department of Electrical Engineering and Computer Science
in partial fulfillment of the requirements for the degree of

MASTER OF SCIENCE

at the

MASSACHUSETTS INSTITUTE OF TECHNOLOGY

September 2023

© 2023 Sabrina M. Corsetti. All rights reserved.

The author hereby grants to MIT a nonexclusive, worldwide, irrevocable, royalty-free license to exercise any and all rights under copyright, including to reproduce, preserve, distribute and publicly display copies of the thesis, or release the thesis under an open-access license.

Authored by:	Sabrina M. Corsetti Department of Electrical Engineering and Computer Science August 31, 2023
Certified by:	Jelena Notaros Robert J. Shillman (1974) Career Development Assistant Professor of Electrical Engineering and Computer Science Thesis Supervisor
Accepted by:	Leslie A. Kolodziejski Professor of Electrical Engineering and Computer Science Chair, Department Committee on Graduate Students

Visible-Light Integrated Photonics for 3D-Printing and Trapped-Ion Systems

by

Sabrina M. Corsetti

Submitted to the Department of Electrical Engineering and Computer Science
on August 31, 2023, in partial fulfillment of the requirements for the degree of

MASTER OF SCIENCE

Abstract

Silicon photonics has enabled next-generation optical technologies that have facilitated revolutionary advances for numerous fields spanning science and engineering, including computing, communications, sensing, and quantum engineering. In recent years, the advent of visible-light integrated photonics platforms has opened up the potential for further diverse applications. This thesis builds upon these recent technologies to demonstrate novel applications of visible-light integrated photonics.

First, we combine the fields of silicon photonics and photochemistry to propose the first chip-based 3D printer, consisting of only a single millimeter-scale photonic chip without any moving parts that emits reconfigurable visible-light holograms up into a simple stationary resin well to enable non-mechanical volumetric 3D printing. This work presents a highly-compact, portable, and low-cost solution for the next generation of 3D printers.

Next, we propose integrated-photonics-based system architectures and the design of key integrated-photonics components for both polarization-gradient and electromagnetically-induced-transparency cooling of trapped ions. Further, we experimentally demonstrate a pair of polarization-diverse gratings and design the first integrated polarization rotators and splitters at blue wavelengths, representing a fundamental stepping stone on the path to advanced operations for integrated-photonics-based trapped-ion quantum systems involving multiple polarizations.

Finally, we demonstrate optical trapping and tweezing of microspheres and cancer cells using an integrated optical phased array for the first time, representing a two-orders-of-magnitude increase in the standoff distance of integrated optical tweezers and the first cell experiments using single-beam integrated optical tweezers.

Thesis Supervisor: Jelena Notaros
Title: Robert J. Shillman (1974) Career Development Assistant Professor of Electrical Engineering and Computer Science

Acknowledgments

First and foremost, I would like to thank my advisor, Professor Jelena Notaros, for providing me with the resources, mentorship, and support required to engage with the work in this thesis. Thank you for introducing me to the incredible field of silicon photonics, for giving me the opportunity to dive into a completely new research field, and for fostering an environment that constantly encourages us to push ourselves to new heights.

Of course, none of this thesis would have been possible without Team PERG, in particular Dianne Lior, whom you can always trust to go to bat for you. I owe an especially huge thank-you to Milica, who has been an amazing mentor. Your patience, kindness, and knowledge/research-sharing have shaped my entire experience in PERG. To the other PERGers (Ashton, Tal, Daniel, Andres, Ben, Henry, and Mikey), thank you for not just enabling the work presented here, but for adding so much to my life in the form of friendship, humor, and support. Ashton and Tal especially, thank you for being two of the best friends a person could ask for, from the very start.

All of the works in this thesis were made possible by the contributions of numerous collaborators. Alex Stafford and Professor Zachariah Page from the UT Austin ZAP Group have generously lent us their resins, expertise, and guidance. The 3D printing project wouldn't be possible without their advances in visible-light photochemistry. The trapped-ion team at MIT/Lincoln Laboratory (Reuel Swint, Gavin N. West, Felix Knollmann, Patrick T. Callahan, Thomas Mahony, Ethan R. Clements, Cheryl Sorace-Agaskar, Dave Kharas, Colin D. Bruzewicz, Robert McConnell, and John Chiaverini) has facilitated every aspect of the quantum systems work, from motivating it with theory, to sharing hardware and software with us, to fabricating our devices. The cells cultured and provided by Kru Kikkeri and Professor Joel Voldman from the RLE Biological Microtechnology and BioMEMS Group were essential for enabling the cell tweezing experiments presented in this work.

This work was supported by the NSF Faculty Early Career Development (CA-

REER) Program (Grant No. 2239525), Defense Advanced Research Projects Agency (DARPA) VIPER program (Grant No. FA8650-17-1-7713), DNSF QLCI HQAN (Grant No. 2016136), NSF QLCI Q-SEnSE (Grant No. 2016244), MIT CQE (Grant No. H98230-19-C-0292), NSF Graduate Research Fellowship Program (Grant No. 1122374), and the MIT Rolf G. Locher Endowed Fellowship.

The MIT RLE, MTL, EECS, and ORCD support infrastructure has made this work possible. The EECS Graduate Office has somehow managed to make me feel like a member of a tight-knit community, despite having over 900 graduate students to account for. I also owe a huge thank-you to the two most critical Bills at MIT: Bill Adams and Bill Gibbs. Thank you both for keeping PERG running, and for being friendly faces around MIT.

I would not be at MIT getting to perform this research were it not for my incredible mentors throughout my time at the University of Michigan. To Professor Tom Schwarz and Dr. Siyuan Sun in particular, you both inspire me not just as advisors/mentors, but as people. I consider myself incredibly lucky to have worked for both of you, and to have you as continued present mentors in my life.

To all of the staff at MIT GradHillel, and to Rabbi Menachem and Mussy Altein at MIT Chabad, thank you for providing a space that always leaves me feeling better than when I entered. To Adina, Will, Seiji, Eva, Arielle, Hugh, Lucy, Lisa, and all of the other wonderful people in GradHillel, Chabad, and Concert Band, thank you for making my time outside the lab just as rewarding as my time in it.

To my cousins, aunts, uncles, and grandparents back home in Illinois, thank you for always making me feel like part of the family unit, even when I'm physically far away. To Marius, thank you for brightening my world every day, even from states away. To my mom and dad, Michelle and Nino, and my brother, Dante, thank you for making me the person I am today. This thesis is a product of your unwavering, constant support for me as I continue to learn and grow.

Contents

1 Introduction **16**

2 Silicon-Photonics-Enabled Chip-Based 3D Printer **19**

2.1 Introduction 19

2.2 The Silicon-Photonics-Enabled Chip-Based 3D Printer Concept . . . 23

2.3 Visible-Light Integrated Optical Phased Array System 24

2.4 Visible-Light-Curable Liquid Resin 26

2.5 Beam-Forming and 3D-Printed Voxel Results 27

2.6 Non-Mechanical Beam-Steering and 3D-Printed Pattern Results . . . 31

2.7 Conclusion 33

3 Integrated Photonics for Trapped-Ion Quantum Systems **36**

3.1 Integrated-Photonics-Based Architectures for Advanced Cooling of Trapped Ions 36

3.1.1 Introduction 36

3.1.2 Integrated-Photonics-Based System Architectures for Trapped-Ion Cooling 37

3.1.3 Conclusion 40

3.2 Integrated Polarization-Diverse Grating Emitters for Trapped-Ion Systems 41

3.2.1 Introduction 41

3.2.2 Grating Design Process and Simulation Results 42

3.2.3 Grating Fabrication and Experimental Results 43

3.2.4 Conclusion 44

3.3 Integrated Visible-Light Polarization Rotators and Splitters for Trapped-Ion Systems 45

3.3.1 Introduction 45

3.3.2 Fabrication Process 46

3.3.3 Adiabatic Polarization Rotator Design 46

3.3.4 Off-Axis Polarization Rotator Design 47

3.3.5 Polarization Splitter Design 48

3.3.6 Conclusion 48

4 Optical Tweezing of Microspheres and Cells Using Integrated Optical Phased Arrays 50

4.1 Introduction 50

4.2 Focusing Integrated Optical Phased Array Architecture 51

4.3 Optical Trapping and Tweezing Results 52

4.4 Conclusion 54

5 Conclusion 57

List of Figures

2.1 Photographs showing (a) a typical commercial 3D printer with a photonic chip (outlined in black) for scale and (b) a fabricated and packaged photonic chip. 20

2.2 (a) Conceptual diagram of the proposed chip-based 3D printer, showing a hologram formed by a chip within a resin chamber (not to scale). (b) Conceptual diagram of the proof-of-concept stereolithography-inspired chip-based 3D printer demonstrated in this chapter (not to scale). . 22

2.3 Top-view simplified schematic of (a) the visible-light liquid-crystal-based cascaded integrated optical phased array that enables the SLA-inspired chip-based 3D-printer system and (b) the vertical-transition escalator from the bottom waveguide to the top waveguide directly underneath the liquid-crystal region. (c) Cross-sectional simplified diagram of the phase shifter after the in-house post-processing packaging steps. (d) Top-view simplified schematic of a cascaded evanescent tap that couples light from the upper bus waveguide to the bottom tap waveguide. (e) Top-view schematic of the grating-based antennas (not to scale). [58, 59] 25

2.4 Photograph of the setup used for the proof-of-concept 3D-printer demonstration, depicting the input fiber, photonic chip, and resin well. . . 28

2.5 (a) Measured far-field radiation pattern emitted by the visible-light integrated optical phased array used for the stereolithography-inspired chip-based 3D printer, showing the main lobe and a grating lobe [59]. (b) Photographs of a 3D-printed voxel, created using the chip-based printer, within a well of remaining liquid resin (top) and the same solid 3D-printed voxel after separation from the remaining liquid resin (bottom). 29

2.6 Measured dimensions for four separate voxels 3D printed with varying printing times of 3, 4, 5, and 10 seconds, demonstrating the formation of voxels as a function of time. 30

2.7 (a) Electrically controlled beam steering of the main lobe of the 3D-printer chip's visible-light integrated optical phased array when a square wave with a varying peak voltage is applied across the liquid-crystal-based phase shifter. (b) Photographs of a 3D-printed line, created using the chip-based printer, within a well of remaining liquid resin (top) and the same solid 3D-printed line after separation from the remaining liquid resin (bottom). 32

2.8 Photographs of a 3D-printed MIT logo, created using the chip-based printer, with a U.S. nickel for scale (left) and zoomed in (right). . . . 33

3.1 Conceptual diagram of the integrated PG-cooling system. 37

3.2 (a) TE grating and (b) TM grating, showing focusing near the height of the ion. 38

3.3 Simplified schematics showing the proposed integrated-photonics-based architectures for (a) TE-TM or TM-TM PG cooling, (b) TE-TE PG cooling, and (c) EIT cooling (not to scale). 39

3.4 (a) Simulated MMI efficiency as a function of MMI length (inset shows device schematic). (b) Simulated phase delay as a function of phase bump width (inset shows device schematic). (c) Simulated conversion efficiency of the off-axis polarization rotator with TE in blue and TM in red (inset shows device schematic). 40

3.5 Simulated xz intensity profiles for the (a) TE and (b) TM grating. . 42

3.6 Micrograph of a fabricated grating. 43

3.7 Experimentally measured xz intensity profiles for the (a) TE and (b) TM grating. Measured spots in the xy plane at $z = 50$ µm for the (c) TE and (d) TM grating. Measured spot profiles in the x (blue) and y (red) dimension at $z = 50$ µm for the (e) TE and (f) TM grating. . . 45

3.8 (a) Schematic (not to scale) of the adiabatic rotator, with relevant mode profiles shown. (b) Mode conversion efficiency of the adiabatic rotator as a function of TE-TM taper length. (c) Schematic of the off-axis rotator, with mode profiles that demonstrate the 45° optical axis rotation of the fundamental modes in the interaction region. (d) Mode conversion efficiency of the off-axis rotator as a function of interaction length. (e) Schematic of the polarization splitter, with mode profiles demonstrating the effective index match and contrast between the fundamental TM and TE modes, respectively. (f) Mode splitting efficiencies for the thru and tap ports for the polarization splitter as a function of interaction length. 47

4.1 (a) Conceptual diagram depicting microsphere tweezing using an OPA by varying the input laser wavelength. (b) Simulated array-factor intensity above the chip for a standard non-focusing OPA (left) and near-field-focusing OPA with a 20-mm focal height (right). (c) Schematic of a passive splitter-tree-based focusing OPA architecture with 4 antennas (not to scale). (d) Element phase distribution for a focusing OPA with a 20-mm focal height, 512 antennas, 2-µm antenna pitch, and 1550-nm wavelength. 52

4.2 (a) Micrograph of microspheres in a sample well with superimposed tracks showing their motion over time (red lines); the motion of the microsphere located at the focal spot of the OPA (circled in white) is significantly reduced compared to its neighbors, indicating successful trapping. (b) Measured trap stiffness versus optical power for polystyrene microsphere trapping; error bars are found by calculating the standard error of the dataset. (c) Micrographs showing the position of a microsphere for input wavelengths of 1550nm (left), 1549nm (center), and 1551nm (right); the position varies with input wavelength, confirming successful tweezing. (d) Position of the spot formed by the optical trap (dashed line) and position of the optically tweezed microsphere (solid line) versus time for two different sinusoidal wavelength control signals, demonstrating consistent tweezing over arbitrary 1D patterns. (e) Micrograph showing a TIB-49 mouse lymphoblast cell trapped in the focus of the optical trap (left); the wavelength of the input laser is reduced by 0.6nm, steering the trap focus in the -y direction below the cell, resulting in the cell being stretched downward by the movement of the trap (right). 54

Chapter 1

Introduction

By leveraging scalable CMOS fabrication techniques to enable chip-based optical microsystems with new functionalities, improved system performance, decreased cost, and reduced size, weight, and power, silicon photonics has enabled next-generation optical technologies that have facilitated revolutionary advances for numerous fields spanning science and engineering, including computing, communications, sensing, and quantum engineering [1–8]. However, motivated by applications such as LiDAR sensing and free-space optical communications, integrated-photonics demonstrations to date have primarily focused on systems that operate at infrared wavelengths.

In recent years, the advent of visible-light integrated-photonics platforms and novel chip-based beam-forming and steering methods has opened up the potential for diverse applications, ranging from augmented reality and display technology to optogenetics [9–13]. In this thesis, we will build upon these recent technologies to introduce 3D printing as a novel application area for visible-light integrated photonics [14], propose integrated-photonics-based system architectures for trapped-ion quantum systems [4] and demonstrate the design and testing of key devices for these architectures [15], and demonstrate integrated-optical-phased-array-based optical trapping and tweezing for the first time [16, 17].

First, in Chapter 2, to address the need for an advanced 3D-printing technology, we combine the fields of silicon photonics and photochemistry to propose the first chip-based 3D printer. The proposed system consists of only a single millimeter-scale photonic chip without any moving parts that emits reconfigurable visible-light holograms up into a simple stationary resin well to enable non-mechanical volumetric 3D printing. Furthermore, we experimentally demonstrate a stereolithography-inspired proof-of-concept version of the chip-based 3D printer using a visible-light beam-steering integrated optical phased array and visible-light-curable resin, showing 3D printing using a chip-based system for the first time. This work demonstrates the first steps towards a highly-compact, portable, and low-cost solution for the next generation of 3D printers.

Second, in Chapter 3, we propose integrated-photonics-based system architectures and the design of key integrated-photonics components for both polarization-gradient and electromagnetically-induced-transparency cooling of trapped ions. Specifically, we design the systems for a wavelength of 422 nm to target the $\mathrm{S}_{1/2}$ to $\mathrm{P}_{1/2}$ transition of $^{88}\mathrm{Sr}^{+}$, a commonly used ion species for trapped-ion qubits. Further, we design and experimentally demonstrate a pair of integrated polarization-diverse gratings, representing the first development of integrated TM-emitting gratings for trapped-ion systems, and, thus, a fundamental stepping stone on the path to advanced operations for integrated-photonics-based trapped-ion quantum systems involving multiple polarizations. Then, we design the first integrated polarization rotators and splitters operating at blue wavelengths; specifically, using combinations of single and dual silicon-nitride waveguide sections, we show an adiabatic polarization rotator, a compact off-axis polarization rotator, and a mode-coupling polarization splitter.

Finally, in Chapter 4, we demonstrate integrated-optical-phased-array-based optical trapping and tweezing for the first time. The optical phased array system focuses emitted light and provides a steerable potential-energy well that can be used to trap and tweeze microscale particles. Using this approach, we increase the standoff distance of integrated optical tweezers by over two orders of magnitude compared to prior demonstrations and show trapping and non-mechanical tweezing of polystyrene microspheres 5 mm above the surface of a silicon-photonic chip. We then use the tweezers to stretch mouse lymphoblast cells, showing, to the best of our knowledge, the first cell experiments using single-beam integrated optical tweezers.

Chapter 2

Silicon-Photonics-Enabled Chip-Based 3D Printer

The following work was done in collaboration with Milica Notaros (MIT), Tal Sneh (MIT), Alex Stafford (UT Austin), Zachariah A. Page (UT Austin), and Jelena Notaros (MIT). This work has been published in [14].

2.1 Introduction

3D printing has transformed modern manufacturing by enabling technologies impacting numerous markets from consumer products to public infrastructure and medicine [18–25]. In recent years, the field has evolved to enable a wide range of print modalities, from high-resolution prints with feature sizes as low as 25nm [26] to the fabrication of large-scale components, spanning rocket engines to bridges [22,27]. As the field of 3D printing has grown to encompass an ever-larger application space, researchers have continued to push the boundaries of the field, developing novel methods for printing.

To date, numerous methods have been commercialized for 3D printing using extrusion, powder-bed fusion, jetting, and light-induced polymerization, among other techniques [28]. At the consumer level, fused deposition modeling (FDM), an extrusion-based method, is the most widely used type of 3D printing [29]. In FDM, parts are

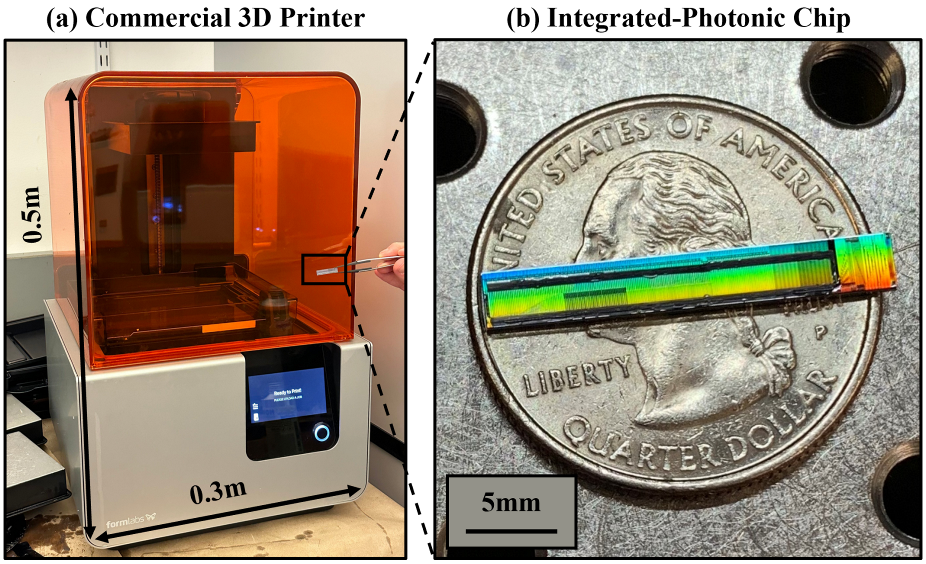
(a) Commercial 3D Printer

(b) Integrated-Photonic Chip

Figure 2.1: Photographs showing (a) a typical commercial 3D printer with a photonic chip (outlined in black) for scale and (b) a fabricated and packaged photonic chip.

built layer by layer by heating and extruding thermoplastic filaments [28, 30]. While FDM has enabled numerous advances in additive manufacturing, especially in regards to rapid prototyping and bioprinting [31, 32], its filament-based approach tends to result in a lower print resolution compared to other common printing methods [33].

In contrast, photocuring-based methods, such as stereolithography (SLA), digital light processing (DLP), and masked stereolithography (MSLA or LCD), offer higher print resolutions, with commercial printers offering feature sizes as low as 10µm [33]. In SLA, a laser beam is used to solidify a pattern into a thin resin layer on a build platform, after which the build platform lifts and a new layer of liquid resin forms. These cycles of curing and platform movement are repeated layer by layer to form a solid 3D object [28, 33, 34]. Similarly, DLP printers also create prints through the layer-by-layer curing of resins. However, while SLA creates prints using a single beam, DLP utilizes the projection of entire 2D images onto a resin's surface, resulting in faster curing [28, 33, 34]. Although these photocuring-based methods enable increased print resolution, they require bulky and complex mechanical systems (Fig. 2.1a), including advanced laser routing schemes (for SLA), anti-aliasing measures (for DLP), specialized build platforms, and precise elevator mechanisms [28, 33–35]. This requirement for large and complex mechanical systems and reliance on layer-by-layer printing limits portability, form factor, resolution, print speed, and material complexity. To combat these challenges, numerous research efforts have been made to push towards new volumetric modalities for 3D printing that benefit from increased build speeds, a lack of reliance on elevator mechanisms, and decreased anisotropy [36–38]. However, these methods still remain reliant on bulky and intricate mechanical systems, such as rotating stages and multi-angle illumination frameworks. Thus, there remains a growing need for a new compact, portable, and low-cost 3D-printing technology.

The field of silicon photonics has the potential to enable a paradigm-shifting solution to address this need for a next-generation 3D-printing technology. By leveraging scalable CMOS fabrication techniques to enable chip-based optical microsystems with new functionalities, improved system performance, decreased cost, and reduced size, weight, and power, silicon photonics has enabled next-generation optical technologies that have facilitated revolutionary advances for numerous fields spanning science and engineering, including computing, communications, sensing, and quantum engineering [1–8]. An emerging class of integrated photonic systems is integrated optical phased arrays, which consist of an array of on-chip optical antennas fed with controlled phases and amplitudes using an integrated photonic circuit, enabling emission and dynamic control of free-space radiated light in a compact form factor, at low costs, and in a non-mechanical way [39–51]. As such, optical-phased-array-based systems have already emerged as a prominent and promising solution for next-generation LiDAR sensors for autonomous vehicles [8, 39, 40]. However, motivated by this initial LiDAR application, integrated-optical-phased-array demonstrations to date have primarily focused on systems that operate at infrared wavelengths, rendering them incompatible with the UV-wavelength-activated photochemistry traditionally used for 3D printing [52]. Integrated optical phased arrays, and the field of silicon photonics in general, have never before been proposed or demonstrated as a solution for 3D printing.

In this chapter, to address this need for an advanced 3D-printing technology, we combine the fields of silicon photonics and photochemistry to propose the first

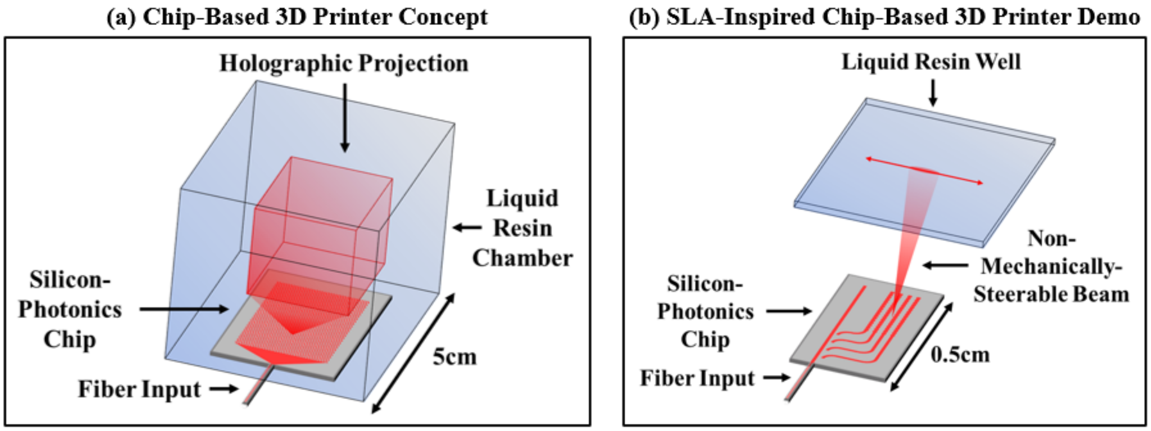
(a) Chip-Based 3D Printer Concept
Holographic Projection
Liquid Resin Chamber
Silicon-Photonics Chip
Fiber Input
5cm
(b) SLA-Inspired Chip-Based 3D Printer Demo
Liquid Resin Well
Non-Mechanically-Steerable Beam
Silicon-Photonics Chip
Fiber Input
0.5cm

Figure 2.2: (a) Conceptual diagram of the proposed chip-based 3D printer, showing a hologram formed by a chip within a resin chamber (not to scale). (b) Conceptual diagram of the proof-of-concept stereolithography-inspired chip-based 3D printer demonstrated in this chapter (not to scale).

chip-based 3D printer. The proposed system consists of only a single millimeter-scale photonic chip without any moving parts that emits reconfigurable visible-light holograms up into a simple stationary resin well to enable non-mechanical volumetric 3D printing (Fig. 2.2a). It presents a highly-compact, portable, and low-cost solution for the next generation of 3D printers.

First, we propose this general chip-based 3D printer concept and outline the key requirements for a complete implementation. Second, as a proof-of-concept demonstration, we experimentally demonstrate a stereolithography-inspired version of this chip-based 3D printer concept by combining the emerging technologies of visible-light integrated optical phased arrays and visible-light-activated photochemistry; the system consists of a visible-light integrated optical phased array that emits and non-mechanically steers a beam up into a well of visible-light-curable resin. Third, we utilize this system to photocure a voxel, thus demonstrating 3D printing using a chip-based system for the first time. Fourth, we characterize the curing rate of this system by measuring the size of individual 3D-printed voxels as a function of curing time, observing printing of sub-millimeter-scale voxels within seconds. Fifth, we utilize the non-mechanical beam-steering capabilities of the system to implement 3D printing of lines in one dimension without any moving parts. Finally, we extend this capability to demonstrate 3D printing of arbitrary patterns in two dimensions using the system.

2.2 The Silicon-Photonics-Enabled Chip-Based 3D Printer Concept

The proposed chip-based 3D printing system consists of a single millimeter-scale silicon-photonics chip sitting at the bottom of a simple stationary well of visible-light-curable liquid resin, as shown in Fig. 2.2a. The proposed chip projects visible-light 3D holograms in the shape of a desired object upwards into the resin well to induce selective solidification of the resin, resulting in a volumetric 3D print. To implement such a system, several key components are required.

The system involves a chamber of liquid resin designed to cure selectively and rapidly when exposed to the visible wavelength of light emitted from the chip [53]. The resin is modular, with the ability to replace the components of the photosystem as required for different wavelengths depending on the desired application [53, 54]. In the proposed system, a silicon-photonics chip sits at the bottom of this chamber and projects a reconfigurable programmable visible-light hologram upwards into the resin, causing the resin to selectively polymerize into a solid print in the shape of the desired object.

The creation of holographic images requires the ability to precisely tune the local phase and amplitude of the light emitted from an aperture [10, 55]. As such, the proposed system incorporates a 2D grid of on-chip visible-light integrated optical phased arrays that act as pixelated emitters, akin to the system demonstrated in [10,12]. Within the proposed system, the phase and amplitude distributions necessary for generating a desired holographic image are closely approximated by discretizing the ideal continuous distributions into local one-dimensional phase gradients with arbitrary amplitudes and absolute phases corresponding to the size of the pixels in the projection system.

To enable routing and emission of light at visible wavelengths, critical for ensuring compatibility with the visible-light-curable resin, the system is based on silicon-nitride waveguides, since silicon nitride has a low absorption coefficient within the visible spectrum and is CMOS compatible. However, silicon nitride has a low thermo-optic coefficient and does not exhibit significant electro-optic properties, which has made integrated modulation at visible wavelengths challenging [56, 57]. As such, liquid-crystal material, with a strong birefringence in the visible spectrum, is integrated into the silicon-photonics platform and used to enable dynamic modulation and encoding of the optical-phased-array-based pixels in the system, as demonstrated in [58, 59].

In the following sections, we develop a proof-of-concept system that serves as a fundamental stepping stone on the path towards this volumetric chip-based 3D-printer vision. Specifically, we experimentally demonstrate a stereolithography-inspired version of the chip-based 3D printer (Fig. 2.1b, 2.2b) capable of 3D printing arbitrary patterns in two dimensions; the system consists of a visible-light integrated optical phased array that emits and non-mechanically steers a beam up into a well of visible-light-curable resin.

2.3 Visible-Light Integrated Optical Phased Array System

As a proof-of-concept demonstration, we develop and experimentally demonstrate a stereolithography-inspired version of the chip-based 3D printer. The system is based on a visible-light integrated optical phased array consisting of a liquid-crystal-based cascaded-phase-shifter architecture that linearly controls the relative phase applied to an array of antennas, as shown in Fig. 2.3a and developed in [59].

At the input, an on-chip inverse-taper edge coupler couples 637-nm-wavelength light from an off-chip laser into an on-chip single-mode 160-nm-thick silicon-nitride waveguide. A 100-µm-long escalator device (an adiabatic layer-transition structure) then couples the input light from the single-mode waveguide into a second 160-nm-

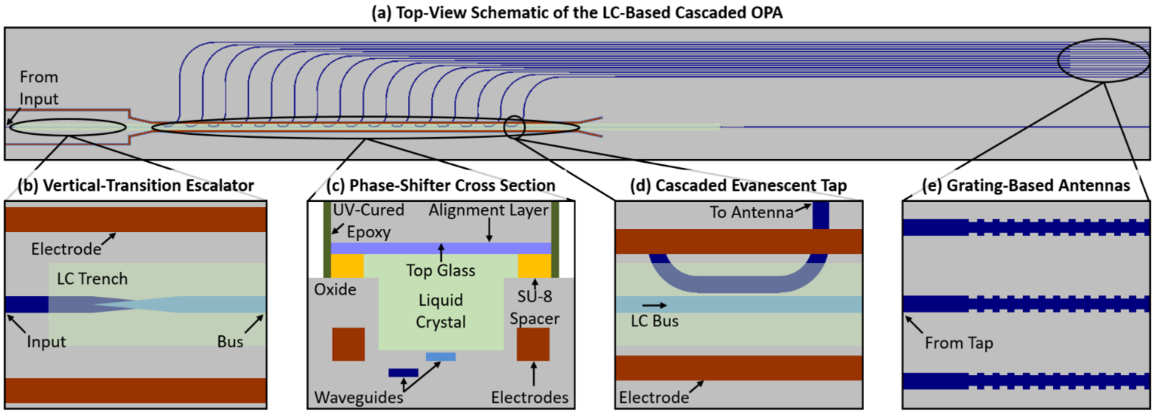
(a) Top-View Schematic of the LC-Based Cascaded OPA
From Input
(b) Vertical-Transition Escalator
Electrode
LC Trench
Input
Bus
(c) Phase-Shifter Cross Section
UV-Cured Epoxy
Alignment Layer
Top Glass
Oxide
Liquid Crystal
SU-8 Spacer
Waveguides
Electrodes
(d) Cascaded Evanescent Tap
To Antenna
LC Bus
Electrode
(e) Grating-Based Antennas
From Tap

Figure 2.3: Top-view simplified schematic of (a) the visible-light liquid-crystal-based cascaded integrated optical phased array that enables the SLA-inspired chip-based 3D-printer system and (b) the vertical-transition escalator from the bottom waveguide to the top waveguide directly underneath the liquid-crystal region. (c) Cross-sectional simplified diagram of the phase shifter after the in-house post-processing packaging steps. (d) Top-view simplified schematic of a cascaded evanescent tap that couples light from the upper bus waveguide to the bottom tap waveguide. (e) Top-view schematic of the grating-based antennas (not to scale). [58, 59]

thick silicon-nitride bus waveguide that is 10nm below a liquid-crystal-filled trench (Fig. 2.3b). Next, evanescent tap couplers, placed with a pitch of 20µm and with increasing coupling lengths, uniformly distribute the light from the bus waveguide to 16 vertically-stacked and horizontally-offset tap waveguides (Fig. 2.3d). These tap waveguides then route to 16 grating-based 400-µm-long antennas with uniform perturbations and a 2-µm pitch to emit the light out of the surface of the chip (Fig. 2.3e).

To enable non-mechanical beam steering, phase modulation of the light emitted out of the array of antennas is required. However, modulation at the visible wavelengths required for this system is difficult because silicon nitride has a low thermo-optic coefficient and does not exhibit significant electro-optic properties [56,57]. Thus, to enable one-dimensional far-field beam steering, the system leverages the birefringence of liquid-crystal medium to enable cascaded phase control to the array of antennas. In a nematic liquid-crystal medium, the refractive index varies based on the orientation of the liquid-crystal molecules with respect to the propagation direction of the light. Thus, by applying an electric field across the liquid-crystal region to orient the molecules in the direction of the applied field, the index of the liquid-crystal media can be actively tuned, resulting in a change in the effective refractive index of the optical mode in the waveguide and a linear phase shift to the antennas. To enable this functionality, the liquid-crystal-based phase-shifting region consists of a silicon-nitride bus waveguide to weakly confine and guide the light, liquid-crystal medium deposited into an 800-nm-deep and 5-µm-wide oxide trench to enable strong interaction between the optical mode and the liquid-crystal medium, 820-nm-thick and 1-µm-wide metal electrodes on each side of the liquid-crystal-filled trench for applying an electric field across the liquid-crystal region, and a top glass chip with a mechanical alignment layer on the underside to anchor the liquid-crystal molecules. A cross-sectional diagram of the phase-shifting region is shown in Fig. 2.3c. Additional details regarding the integrated optical phased array and the integrated liquid-crystal modulators are provided in [58, 59].

This liquid-crystal-based cascaded integrated optical phased array was fabricated in a CMOS-compatible 300-mm wafer-scale silicon-photonics process at the State University of New York Polytechnic Institute's (SUNY Poly) Albany NanoTech Complex. We then diced the fabricated photonic wafer and performed a chip-scale liquid-crystal-packaging process at MIT. Further fabrication and packaging details are provided in [58, 60].

2.4 Visible-Light-Curable Liquid Resin

The resin used in the stereolithography-inspired proof-of-concept demonstration of the chip-based 3D printer is a three-component-photosystem-based resin designed for efficient photocuring at visible wavelengths, as developed in [53, 54].

Typical resin photosystems rely on either a single photoinitiator or a combination of a photocatalyst and either a hydrogen donor or an electron donor/acceptor. In the latter case, photocuring occurs by electron transfer from a photoredox catalyst to a coinitiator, followed by bond scission to generate radicals or ions that initiate polymerization [61–65]. While the use of a photoredox compound enables photocuring via excitation of a $\pi \to \pi^*$ transition with high attenuation at visible wavelengths

(>500nm), photosystems of this kind typically exhibit long curing times (>60s) due to their multistep reaction mechanisms. To combat this, we use a three-component photosystem in this work [53], consisting of a photoredox compound and a pair of coinitiators, rather than a single coinitiator. The presence of the two coinitiators enables curing that promotes both photoredox compound regeneration and doubles the concentration of radicals produced per photon absorbed, as detailed in [53].

To create the resin used in this work, we first synthesize the photoredox compound (aza-Br) – an aza-boron-dipyrromethene (Aza-BODIPY) dye – using acetophenone and benzaldehyde derivatives as well as N-bromosuccinimide, in a process detailed in [54]. During the synthesis process, we halogenate the BODIPY to increase its intersystem crossing rate to long-lived triplet excited states, further improving the reaction efficiency of the photosystem by increasing the number of collisions between initiators and excited photoredox compounds per photon absorbed [66]. The resulting aza-Br compound exhibits peak extinction around 660nm, enabling compatibility with the chip-based 3D printer's operating wavelength of 637nm [54]. To complete the photosystem, we combine the aza-Br (7.6mg, 0.4 mol%) with a coinitiator pair of Borate V (3.8mg, 0.4 mol%) and H-Nu 254 (52.0mg, 4.0 mol%). Finally, we fully dissolve the photosystem in a 10:1 mixture of tetraethylene glycol diacrylate (0.7mL) and trimethylolpropane triacrylate (0.07mL) to create the complete resin. We dissolve the photosystem in a dark environment to avoid unnecessary onset of polymerization.

2.5 Beam-Forming and 3D-Printed Voxel Results

Using the visible-light integrated optical phased array and the visible-light-curable resin described above, we demonstrate 3D printing using a chip-based system for the first time.

The setup used for this printing demonstration is shown in Fig. 2.4. The fabricated and packaged 3D-printer photonic chip is mounted on a chuck, with a sample stage that supports liquid resin wells mounted on a positioning system above the chip. Light is routed from an off-chip diode laser centered at 637nm via a P1-630Y cleaved

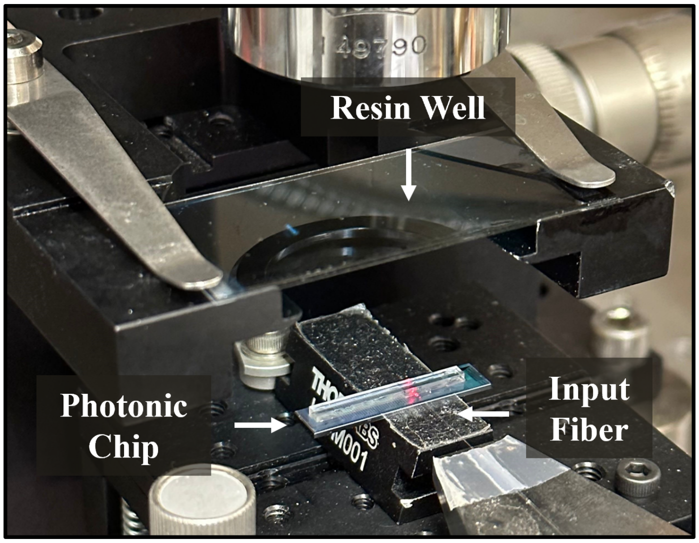

Figure 2.4: Photograph of the setup used for the proof-of-concept 3D-printer demonstration, depicting the input fiber, photonic chip, and resin well.

fiber and is edge coupled to the on-chip system. The setup is visualized using a 10x Mitutoyo objective, and split into both near- and far-field imaging paths using a visible beam splitter and focusing lens. Using this setup, we image the beam emitted by the integrated optical phased array in the far field, resulting in the pattern depicted in Fig. 2.5a. The beam is elliptical with a power full-width half maximum of 0.4° × 1.6°, due to the difference in aperture size between the antenna and array dimensions. Further details regarding integrated-optical-phased-array radiation-pattern characterization are provided in [59].

To create a well for the liquid resin, two coverslips are separated by one layer of double-sided tape on the left-hand side of the well and one layer of single-sided tape on the right-hand side of the well to ensure that the coverslips are securely attached, while also creating an easy-access hinge for removing cured prints from the well. This creates a chamber with a thickness of approximately 60µm into which 55µL of liquid resin is pipetted. The well containing the resin is then clamped into the sample stage above the chip and centered on the main lobe emitted by the integrated optical phased array. Resin preparation and 3D printing are performed in a dark environment to prevent curing from visible-light sources other than the integrated optical phased array.

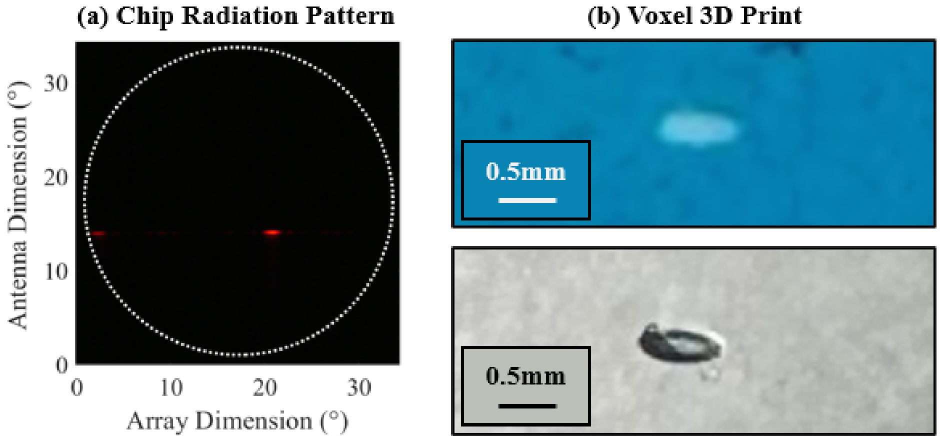

Figure 2.5: (a) Measured far-field radiation pattern emitted by the visible-light integrated optical phased array used for the stereolithography-inspired chip-based 3D printer, showing the main lobe and a grating lobe [59]. (b) Photographs of a 3D-printed voxel, created using the chip-based printer, within a well of remaining liquid resin (top) and the same solid 3D-printed voxel after separation from the remaining liquid resin (bottom).

After centering the resin sample on the main lobe of the integrated optical phased array, we use the visible-light microscope path to monitor curing, which is observable via diffraction of the integrated optical phased array's radiation pattern around a solidified voxel. As depicted in Fig. 2.5b, a 3D-printed voxel presents as a bleached region (white/transparent) within remaining leftover resin (blue) due to photobleaching of the blue aza-Br photoredox compound during the photocuring reaction. Using a Kim wipe and isopropyl alcohol, we separate the cured print from the remaining uncured liquid resin. The result is a free-standing 3D-printed voxel in the shape of the integrated optical phased array's main lobe (Fig. 2.5a). The single voxel depicted in Fig. 2.5b measures approximately 0.5mm × 0.125mm in the plane of the photograph with a height of approximately 60µm. The voxel height is determined by the spacing of the resin well's coverslips (60µm for this test). The planar dimensions of the voxel are determined by the distance between the integrated optical phased array and the resin well, since the integrated optical phased array used for this proof-of-concept 3D printer emits a diffracting beam (0.4° × 1.6°). In this demonstration, we placed the resin well 2.5cm over the surface of the 3D-printer chip, resulting in sub-millimeter-

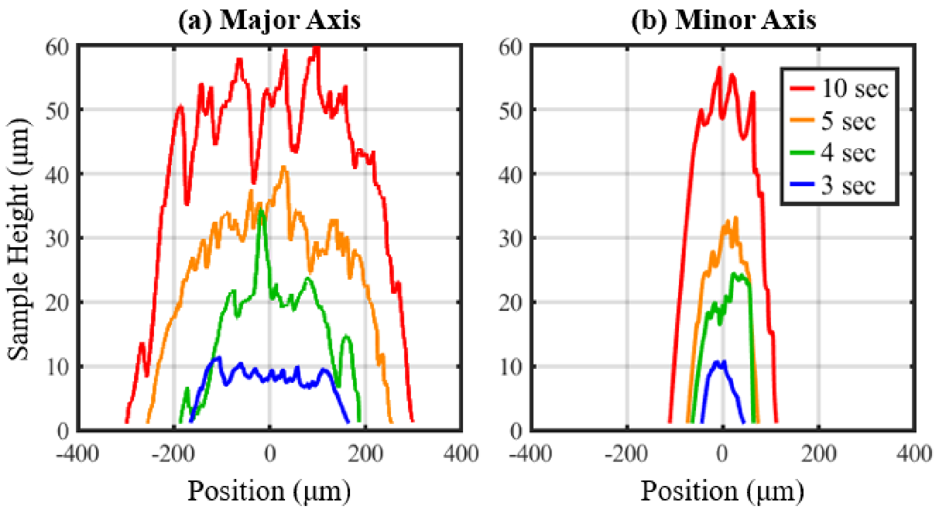

Figure 2.6: Measured dimensions for four separate voxels 3D printed with varying printing times of 3, 4, 5, and 10 seconds, demonstrating the formation of voxels as a function of time.

scale voxels (Fig. 2.5b, 2.6). The use of focusing integrated optical phased arrays developed by our group [12] in future iterations of the chip-based 3D printer would enable printing of even smaller micron-scale voxels.

To characterize the curing rate and print formation process of these voxel prints, we performed curing and profilometry for 3D prints with varying curing time intervals (Fig. 2.6). Specifically, we 3D printed four single voxels using four separate resin wells with varying printing times of 3, 4, 5, and 10 seconds. After separating the resulting voxels from the remaining liquid resin, we used a Veeco Dektak 150 Surface Profilometer to measure the height of the prints along their major and minor (longer and shorter) axes. As depicted in Fig. 2.6, we find that 3D-printed voxels grow as a function of time, eventually reaching a plateau upon growing to the top of the resin well, at a height of approximately 60µm. To demonstrate the rapid curing capability of the system for this test, we set the power of the off-chip diode laser such that approximately 6.7µW of optical power was supplied to the main lobe of the integrated optical phased array. At this power, we observe voxel printing within seconds (Fig. 2.6). Even at significantly lower optical powers on the order of 100pW, we can still observe voxel formation within 10 minutes, with a nonlinear relationship between optical power and printing time [53, 54].

2.6 Non-Mechanical Beam-Steering and 3D-Printed Pattern Results

Utilizing the non-mechanical beam-steering capabilities of the visible-light integrated optical phased array, we then moved beyond the printing of single voxels and demonstrated 3D printing of one- and two-dimensional patterns.

To enable non-mechanical beam steering in the array dimension of the integrated optical phased array, we use electronic probes to contact the photonic chip's integrated electrodes and apply a 10-kHz square wave across the electrodes of the liquid-crystal phase shifter. We vary the peak voltage of this applied square wave to tune the phase gradient applied across the antennas and, hence, steer the formed beam in the array dimension by up to 7.2° within ±3.4V. as shown in Fig. 2.7a. Further details regarding integrated-optical-phased-array beam-steering characterization are provided in [59].

Using this non-mechanical beam-steering capability, we demonstrate 3D printing of a line into the resin, as shown in Fig. 2.7b. We print this line by sweeping the voltage applied to the liquid-crystal phase shifter from $0\mathrm{V_p}$ to $3\mathrm{V_p}$. As the voltage applied to the phase shifter is increased, the refractive index of the liquid crystal relative to the mode in the phase shifter increases, leading to lower confinement of the mode in the bus waveguide. As a result, the power delivered to the integrated optical phased array antennas decreases as the radiation pattern steers. To compensate for this, we print for longer times at higher voltages than for lower voltages, to ensure uniform curing along the line. As depicted in Fig. 2.7b, the 3D-printed line is distinguishable from the remaining blue liquid resin, as in the case of the single-voxel print in Fig. 2.5b. We again separate the print from the remaining liquid using a Kim wipe and isopropyl alcohol, and we demonstrate that the result is once again a free-standing 3D-printed solid.

Using single-line prints as a building block, we now demonstrate the system's ability to 3D print arbitrary patterns in two dimensions, thus realizing our proof-of-concept stereolithography-inspired chip-based 3D printer system. To transition from single-line prints to arbitrary two-dimensional patterns, we use the resin well's

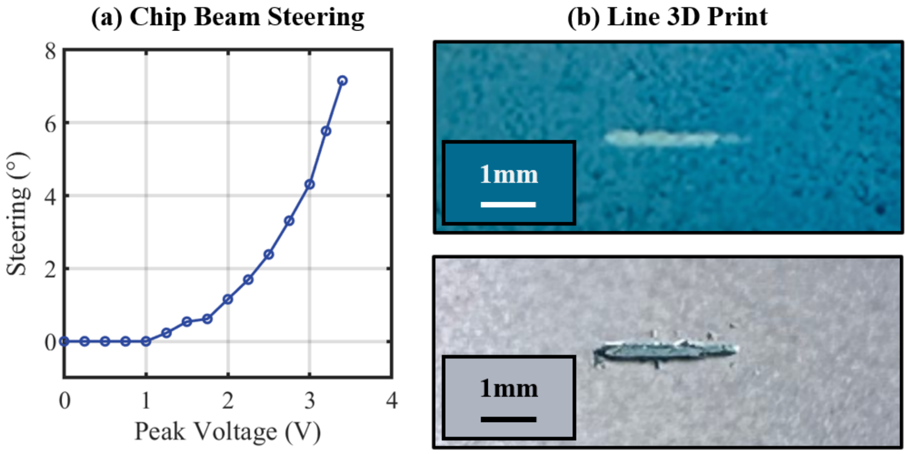

Figure 2.7: (a) Electrically controlled beam steering of the main lobe of the 3D-printer chip's visible-light integrated optical phased array when a square wave with a varying peak voltage is applied across the liquid-crystal-based phase shifter. (b) Photographs of a 3D-printed line, created using the chip-based printer, within a well of remaining liquid resin (top) and the same solid 3D-printed line after separation from the remaining liquid resin (bottom).

mechanical positioning stage. Specifically, after printing each one-dimensional line in a desired pattern, we use the mechanical stage to move the well with micron-scale precision in the second dimension. As a specific demonstration, we perform a print of the Massachusetts Institute of Technology (MIT) logo, creating each line in the print from a subset of the single-line voltage range (0-3V_p). To promote rapid yet controlled printing for this demonstration, we set the power of the off-chip diode laser such that approximately 1.9µW of optical power was supplied to the main lobe of the integrated optical phased array. Between each line of the print, we decrease the integrated optical phased array's output power to prevent curing between components. As oxygen in the sample is quenched during the print, the curing rate becomes faster [53]. We thus adapt the amount of time spent on each component of the logo to ensure uniform curing (e.g., printing the vertical component of the "T" in the logo faster than the bottom component of the "I"). The final print, performed in under 6 minutes total, is depicted in Fig. 2.8, once again separated from any remaining liquid resin using a Kim wipe and isopropyl alcohol.

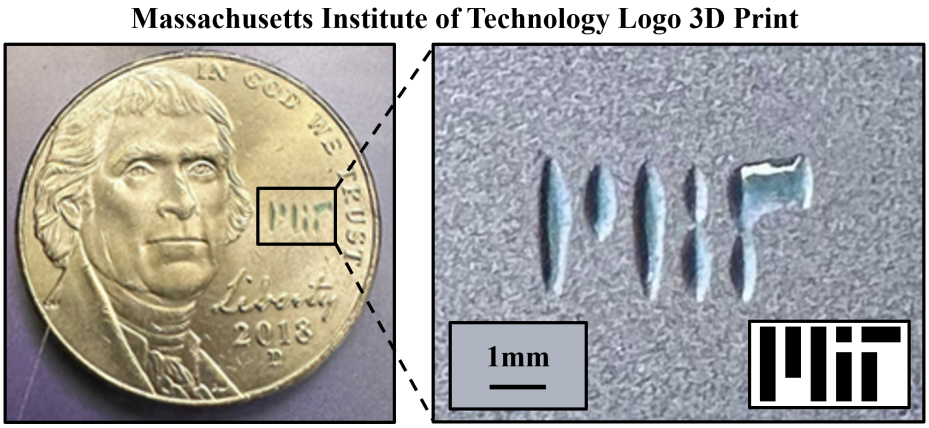
Massachusetts Institute of Technology Logo 3D Print

Figure 2.8: Photographs of a 3D-printed MIT logo, created using the chip-based printer, with a U.S. nickel for scale (left) and zoomed in (right).

2.7 Conclusion

This chapter combines the fields of silicon photonics and photochemistry to propose the first chip-based 3D-printing technology. The proposed system consists of only a single millimeter-scale photonic chip without any moving parts that emits reconfigurable visible-light holograms up into a simple stationary resin well to enable non-mechanical volumetric 3D printing.

First, we proposed this general chip-based 3D printer concept and outlined the key requirements for a complete implementation. Second, as a proof-of-concept demonstration, we experimentally demonstrated a stereolithography-inspired version of this chip-based 3D printer concept by combining the emerging technologies of visible-light integrated optical phased arrays and visible-light-activated photochemistry; the system consists of a visible-light integrated optical phased array that emits and non-mechanically steers a beam up into a well of visible-light-curable resin. Third, we utilized this system to photocure a voxel, thus demonstrating 3D printing using a chip-based system for the first time. Fourth, we characterized the curing rate of this system by measuring the size of individual 3D-printed voxels as a function of curing time, observing printing of sub-millimeter-scale voxels within seconds. Fifth, we utilized the non-mechanical beam-steering capabilities of the system to implement 3D printing of lines in one dimension without any moving parts. Finally, we extended this capability to demonstrate 3D printing of arbitrary patterns in two dimensions using the system. In the future, we will utilize a holographic visible-light optical-phased-array-based system [10] to extend this work and demonstrate the complete volumetric chip-based 3D printer concept.

The chip-based 3D-printing technology introduced in this chapter has the potential to enable a highly-compact, portable, and low-cost solution for the next generation of 3D printers. Such a solution would offer a more accessible and rapid mechanism for generating 3D objects, impacting a wide range of application areas, including military, medical, engineering, and consumer.

Chapter 3

Integrated Photonics for Trapped-Ion Quantum Systems

3.1 Integrated-Photonics-Based Architectures for Advanced Cooling of Trapped Ions

The following work was done in collaboration with Ashton Hattori (MIT), Tal Sneh (MIT), Milica Notaros (MIT), Reuel Swint (MIT Lincoln Laboratory), Patrick T. Callahan (MIT Lincoln Laboratory), Colin D. Bruzewicz (MIT Lincoln Laboratory), Felix Knollmann (MIT), Robert McConnell (MIT Lincoln Laboratory), John Chiaverini (MIT Lincoln Laboratory), and Jelena Notaros (MIT). This work has been published in [4].

3.1.1 Introduction

Systems of trapped ions are a promising modality for quantum information processing due to their long coherence times and strong ion-ion interactions, which enable high-fidelity two-qubit gates [67]. Most current implementations are comprised of complex free-space optical systems, whose large size and susceptibility to vibrations and drift can limit fidelity and addressability of ion arrays, hindering scaling to large numbers of qubits. Recent works based on integrated photonic devices offer a potential avenue to address many of these challenges [3–5, 68].

Motional state cooling is a key optical function in trapped-ion systems. To date, integrated-photonics-based cooling demonstrations have been limited to Doppler and resolved-sideband cooling [3, 68]. However, polarization-gradient (PG) and electromagnetically-induced-transparency (EIT) cooling can offer better cooling performance in multi-ion systems, where sub-Doppler temperatures in several non-degenerate modes are desirable. While free-space demonstrations of these cooling schemes have been shown [69,70], each having an advantage for differing applications, integrated versions of these systems have not yet been realized.

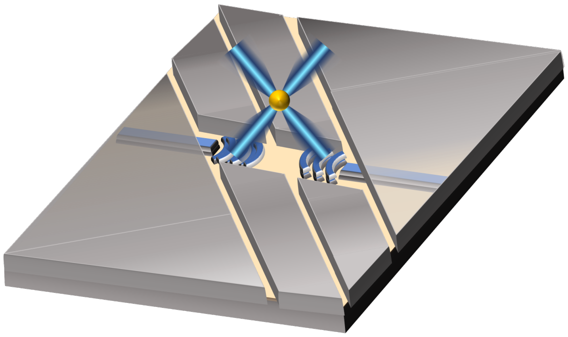
Conceptual Diagram

Figure 3.1: Conceptual diagram of the integrated PG-cooling system.

In this section, we propose integrated-photonics-based system architectures and the design of key integrated photonic components for both PG and EIT cooling of trapped ions (conceptual diagram shown in Fig. 3.1). Specifically, we design the systems for a wavelength of 422 nm to target the $S_{1/2}$ to $P_{1/2}$ transition of $^{88}Sr^{+}$, a commonly used ion species for trapped-ion qubits.

3.1.2 Integrated-Photonics-Based System Architectures for Trapped-Ion Cooling

We leverage a 200-mm wafer-scale visible-wavelength process developed at MIT Lincoln Laboratory to enable low-loss waveguide fabrication over a wavelength range relevant to commonly used ion species [13]. The platform consists of two bottom lay-

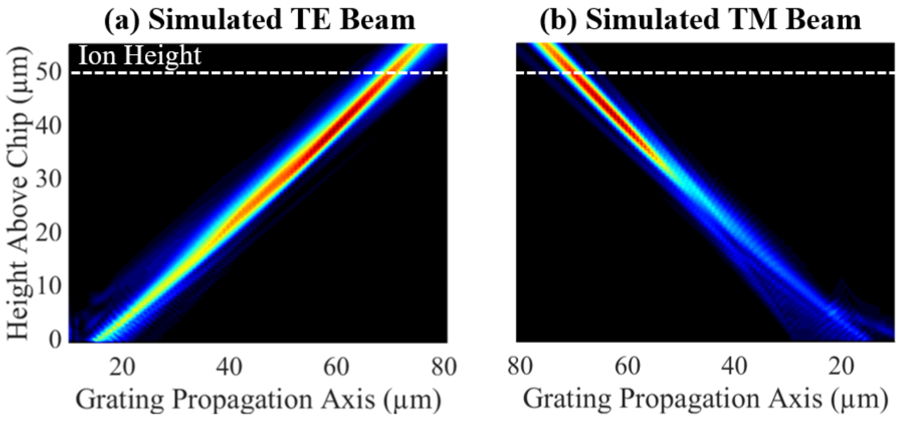

Figure 3.2: (a) TE grating and (b) TM grating, showing focusing near the height of the ion.

ers of 100-nm-thick silicon nitride (Si_3N_4) and an upper layer of 100-nm-thick alumina (Al_2O_3) separated by 90 nm of silicon dioxide (SiO_2). A top metal layer is etched to create linear-ion-trap electrodes that confine ions 50 µm above the trap surface via radiofrequency and DC voltages [67].

Trapped ions located in a suitable laser-polarization gradient can achieve sub-Doppler temperatures due to the preferential scattering of cooling photons in a spatially-varying, state-dependent energy potential [69]. Appropriate polarization gradients can be realized on-chip using different configurations of integrated grating couplers; for example, two transverse-electric (TE) gratings placed orthogonal to each other (TE-TE), a TE and transverse-magnetic (TM) grating placed opposite to each other (TE-TM), or two TM gratings placed opposite to each other (TM-TM) all suffice. The simulated emission profiles for gratings specifically designed for TE and TM are shown in Fig. 3.2a–b (introduced in detail in Sec. 3.2). Both gratings are designed to match intensity and focus near the ion at an angle of 45°, maximizing intensity at the ion location. In all three polarization configurations, light is routed to these gratings via two separate inverse-taper edge couplers and a combination of 650-nm-wide alumina waveguides, 300-nm-wide dual-layer silicon-nitride waveguides, and vertical transitions between layers. The final proposed architectures for PG cooling are shown in Fig. 3.3a–b.

EIT cooling enables near ground-state cooling over a wide frequency range by

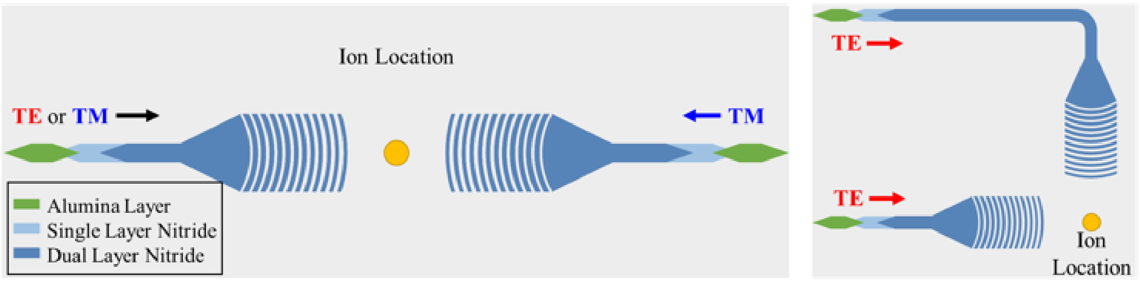
(a) TE-TM or TM-TM PGC Schematic

(b) TE-TE PGC Schematic

Ion Location
TE or TM
TM
Alumina Layer
Single Layer Nitride
Dual Layer Nitride
TE
TE
Ion Location

(c) EIT Cooling Schematic

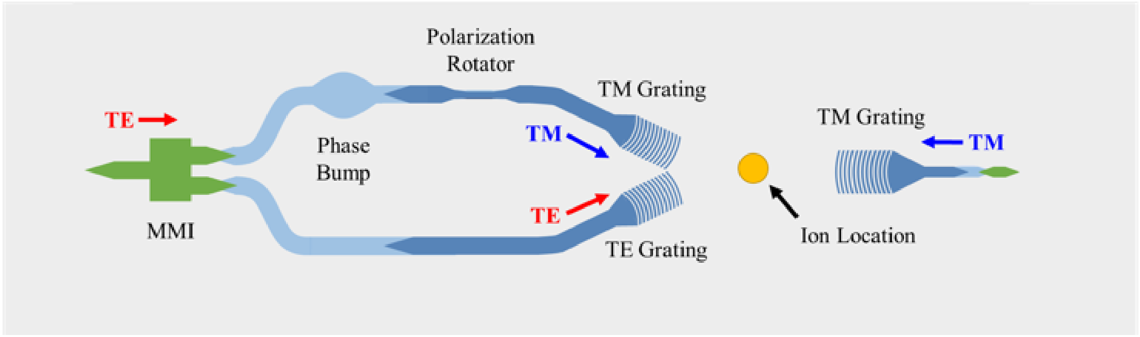
Polarization Rotator
TM Grating
TE
Phase Bump
TM
TE
MMI
TE Grating
TM Grating
TM
Ion Location

Figure 3.3: Simplified schematics showing the proposed integrated-photonics-based architectures for (a) TE-TM or TM-TM PG cooling, (b) TE-TE PG cooling, and (c) EIT cooling (not to scale).

suppressing unwanted heating mechanisms otherwise incurred during laser cooling. Previous free-space demonstrations have relied on two appropriately-polarized laser sources (one circular and one linear) to create the desired laser absorption profile [70].

Fig. 3.3c depicts integrated realization of both the circular and linear sources. To generate the circularly polarized source, light is coupled on chip via an inverse-taper edge coupler to an alumina waveguide. Next, the light is split evenly into two arms using a 32.2-µm-long 1x2 alumina multi-mode interferometer (MMI); simulated efficiency as a function of device length for the MMI is shown in Fig. 3.4a. In the upper arm, the light is transitioned to single-layer silicon nitride. Then, the waveguide is adiabatically widened for a given length, forming a phase bump to impart a 90° phase shift; simulated phase as a function of bump width is shown in Fig. 3.4b. After passing through the phase bump, the light is transitioned to dual-layer nitride. There, it goes through an off-axis polarization rotator, which rotates the incoming light from TE to TM (introduced in detail in Sec. 3.3); the conversion efficiency as a function of

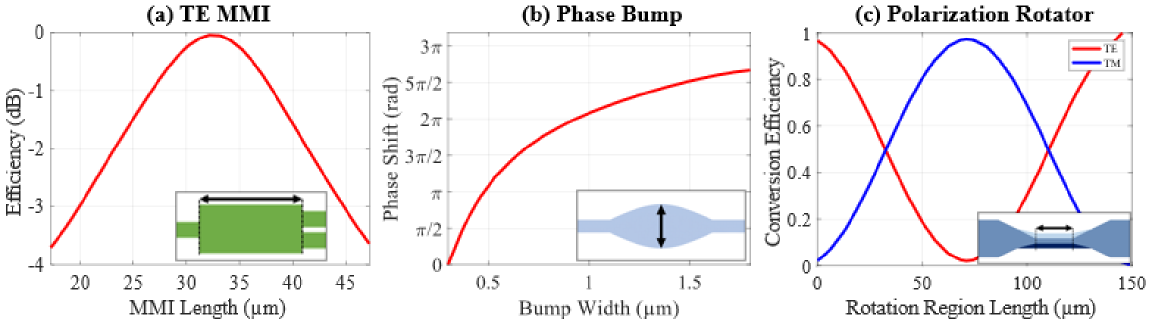

Figure 3.4: (a) Simulated MMI efficiency as a function of MMI length (inset shows device schematic). (b) Simulated phase delay as a function of phase bump width (inset shows device schematic). (c) Simulated conversion efficiency of the off-axis polarization rotator with TE in blue and TM in red (inset shows device schematic).

device length can be seen in Fig. 3.4c, with a peak simulated conversion efficiency of 99.15% [15]. Finally, the TM light in the upper arm is emitted via a TM grating. In the lower arm from the MMI, the TE light is transitioned to dual-layer nitride and is emitted via a TE grating. The two gratings in each arm are angled so that the beams combine and form approximately circularly polarized light at the ion location. The linear TM input is coupled on-chip from an inverse-taper edge coupler into an alumina waveguide. Next, it is transitioned to dual-layer silicon nitride, where it emits from a focusing TM grating placed opposite to the circularly polarized source, thus enabling EIT cooling.

3.1.3 Conclusion

In this section, we have developed a framework for two advanced trapped-ion cooling schemes, PG and EIT, using a visible-wavelength silicon-photonics platform at 422 nm. We have also developed designs of key integrated-photonics components required to realize these architectures. This approach provides a scalable platform that promises more rapid cooling of multiple vibrational modes when compared to previously shown integrated approaches. Additionally, these approaches should be applicable to neutral-atom laser cooling when tailored to other wavelengths.

3.2 Integrated Polarization-Diverse Grating Emitters for Trapped-Ion Systems

The following work was done in collaboration with Ashton Hattori (MIT), Reuel Swint (MIT Lincoln Laboratory), Milica Notaros (MIT), Gavin N. West (MIT), Tal Sneh (MIT), Felix Knollmann (MIT), Patrick T. Callahan (MIT Lincoln Laboratory), Thomas Mahony (MIT Lincoln Laboratory), Ethan R. Clements (MIT), Cheryl Sorace-Agaskar (MIT Lincoln Laboratory), Dave Kharas (MIT Lincoln Laboratory), Robert McConnell (MIT Lincoln Laboratory), John Chiaverini (MIT Lincoln Laboratory), and Jelena Notaros (MIT).

3.2.1 Introduction

As discussed in Section 3.1.1, systems of trapped ions are a promising modality for quantum information processing due to their long coherence times and strong ion-ion interactions, which enable high-fidelity two-qubit gates [67]. However, most current implementations are comprised of complex free-space optical systems, whose large size and susceptibility to vibrations and drift can limit fidelity and addressability of ion arrays, hindering scaling to large numbers of qubits. Recently, integrated-photonics-based devices and systems have been demonstrated as an avenue to address these challenges [3, 68].

To date, these prior integrated demonstrations have been limited to operations using light of only a single linear polarization, specifically transverse electric (TE), nominally parallel to the ion-trap chip surface. However, diverse polarizations are critical for enabling numerous operations for advanced trapped-ion systems, leading to an interest in developing polarization-diverse emitters [71, 72]. For example, integrated-photonics-based architectures involving light of both TE and transverse-magnetic (TM) polarizations (such as the configuration in Fig. 3.1) are necessary for enabling advanced ion cooling schemes that offer sub-Doppler temperatures over several non-degenerate trap-vibrational modes, such as polarization-gradient and electromagnetically-induced-transparency cooling, as discussed in Section 3.1 [4].

In this section, we design and experimentally demonstrate a pair of integrated TE- and TM-emitting gratings with an operating wavelength of 422 nm, corresponding to the $5^2S_{1/2}$ to $5^2P_{1/2}$ transition of $^{88}Sr^+$ ions, a key transition for ion control. We implement a custom optimization-based design algorithm to realize bilayer, apodized, and curved gratings that emit unidirectional focused beams, with experimentally measured spot dimensions of 7.6 µm × 4.3 µm for the TE grating and 5.0 µm × 3.6 µm for the TM grating at a target ion height of 50 µm above the surface of the chip. This work represents, to the best of our knowledge, the first development of integrated TM-emitting gratings for trapped-ion systems, and, thus, a fundamental stepping stone on the path to advanced operations for integrated-photonics-based trapped-ion quantum systems involving multiple polarizations.

3.2.2 Grating Design Process and Simulation Results

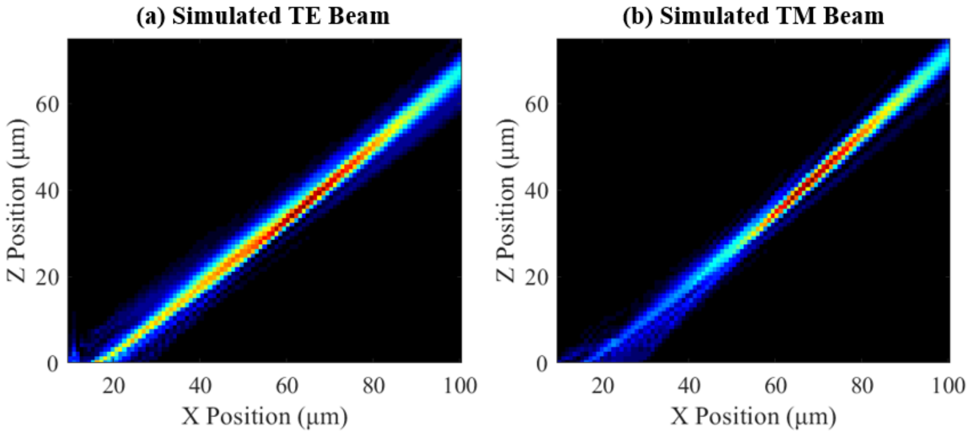

Figure 3.5: Simulated xz intensity profiles for the (a) TE and (b) TM grating.

Both of the gratings in this section are comprised of two 100-nm-thick layers of silicon nitride separated by 90 nm of silicon dioxide, with the grating teeth fully etched into the nitride. The pitch and duty cycles of each layer's grating teeth are optimized such that the gratings emit focused beam profiles that maximize the percentage of light emitted towards a target ion location 50 µm above the surface of the chip. In addition, the teeth in each layer are offset from each other in the propagation dimension (x) to enable unidirectional emission upwards [73]. Finally, the grating teeth are curved to enable focusing in the transverse dimension (y) of the grating.

To design each grating, we utilize a particle swarm algorithm to determine the optimal pitches, duty cycles, and offsets of the teeth in both layers. Then, we use a slab mode simulation to determine the optimal grating tooth curvature, based on the phase front of the mode propagating in the grating. Finally, we simulate the grating and compute its expected emission angle, beam dimensions, and efficiency.

The gratings developed in this work are designed with a 17 µm × 18 µm emitting aperture area. This size was chosen such that the optimized TE and TM gratings emit with matching efficiencies — a necessary condition for many ion operations involving both polarizations, such as polarization-gradient cooling [4]. The resulting simulated emission profiles in the xz plane for both gratings are plotted in Fig. 3.5a–b. The TE grating has an expected emission angle of 48.6° and a spot size (1/e^2 diameter) of 9.9 µm × 5.0 µm at the ion location 50 µm above the chip surface. The TM grating has an expected emission angle of 47.8° and a spot size of 6.1 µm × 3.7 µm at the ion location 50 µm above the chip surface.

3.2.3 Grating Fabrication and Experimental Results

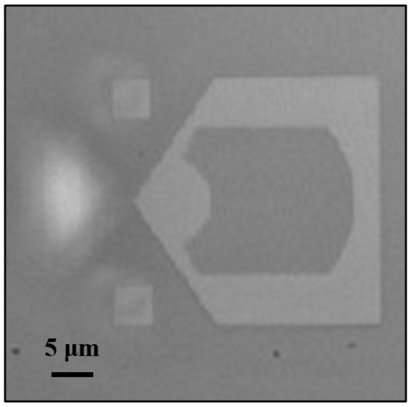

Figure 3.6: Micrograph of a fabricated grating.

The designed gratings were fabricated in our 200-mm wafer-scale fabrication process developed at MIT Lincoln Laboratory for wavelengths spanning the range from ultraviolet to near infrared (Fig. 3.6) [13].

To characterize the gratings, light is routed to the chip from a benchtop laser source through a series of polarization-maintaining fibers. At the chip facet, we use a polarizing beam-splitter cube on a mount aligned with the axes of the chip to align the incident polarization of the fiber to the operating polarization of the measured grating (either TE or TM). The light from the fiber is then coupled onto the chip using an on-chip tapered edge coupler, and light is routed to the gratings using a combination of alumina waveguides, silicon-nitride waveguides, and vertical transitions between layers [13]. To measure each grating's performance, we visualize the chip with a 50X objective and a visible-light camera, and use an automated setup to increment the height of the optical train in 1-µm steps to capture images of the grating's emitted beam over a range of 0 to 100 µm above the surface of the chip (Fig. 3.7a–b). We then use the resulting data to compute the grating's emission angle and beam dimensions (Fig. 3.7c–f).

Using this characterization procedure, we find that the fabricated TE grating successfully emits TE-polarized light at an angle of 43.2° (Fig. 3.7a) with a spot size ($1/e^2$ diameter) of 7.6 µm × 4.3 µm at 50 µm above the chip (Fig. 3.7c,e). Similarly, the fabricated TM grating successfully emits TM-polarized light at an angle of 43.1° (Fig. 3.7b) with a spot size of 5.0 µm × 3.6 µm at 50 µm above the chip surface (Fig. 3.7d,f).

3.2.4 Conclusion

In this section, we designed and experimentally demonstrated a pair of integrated TE- and TM-emitting gratings with an operating wavelength of 422 nm, corresponding to the $5^2S_{1/2}$ to $5^2P_{1/2}$ transition of $^{88}Sr^+$ ions. This work represents, to the best of our knowledge, the first development of integrated TM-emitting gratings for trapped-ion systems, and, thus, a fundamental stepping stone on the path to advanced operations for trapped-ion quantum systems involving multiple polarizations, such as polarization-gradient and electromagnetically-induced-transparency cooling [4,15], using an integrated photonics platform.

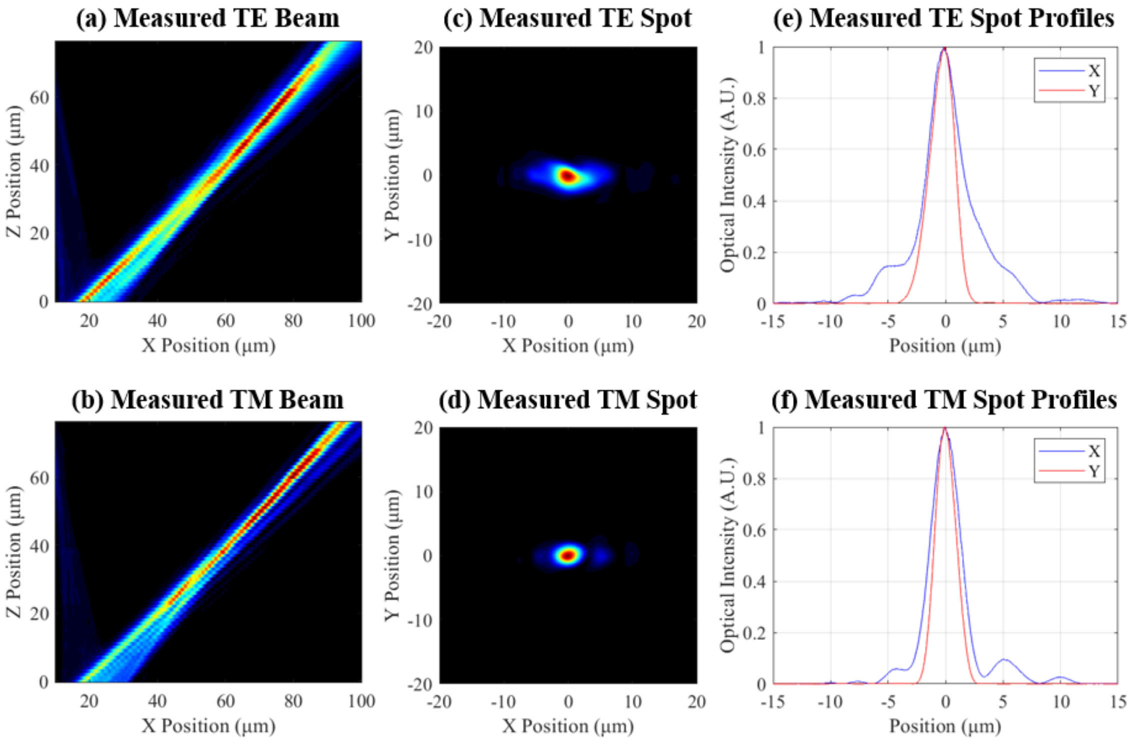

Figure 3.7: Experimentally measured xz intensity profiles for the (a) TE and (b) TM grating. Measured spots in the xy plane at $z = 50$ µm for the (c) TE and (d) TM grating. Measured spot profiles in the x (blue) and y (red) dimension at $z = 50$ µm for the (e) TE and (f) TM grating.

3.3 Integrated Visible-Light Polarization Rotators and Splitters for Trapped-Ion Systems

The following work was led by Tal Sneh (MIT) and Ashton Hattori (MIT) and done in collaboration with Milica Notaros (MIT) and Jelena Notaros (MIT). This work has been published in [15].

3.3.1 Introduction

Polarization control plays an important role in photonic integrated circuits (PICs), where it can enhance polarization-sensitive device performance as well as enable systems that can benefit from orthogonal modes, such as increased channel density for communications [74, 75]. As such, there has been extensive research into integrated polarization rotators and splitters [75–79]; so far, however, they have primarily been shown at infrared (IR) wavelengths.

Recently, there has been a significant drive to develop PICs at visible wavelengths that require polarization manipulation, in particular for chip-scale atomic systems and qubit state preparation [3, 79] (discussed in Sec. 3.1). However, integrated polarization-control devices for these systems have yet to be developed, a particular challenge given the scaling of device dimensions with wavelength.

In this section, we demonstrate the design of the first integrated polarization rotators and splitters operating at blue wavelengths. Specifically, using combinations of single and dual silicon-nitride (SiN) waveguide sections, we show an adiabatic polarization rotator, a compact off-axis polarization rotator, and a mode-coupling polarization splitter all operating at a wavelength of 422 nm.

3.3.2 Fabrication Process

Similar to the above sections, the devices in this work were designed for fabrication compatibility with the MIT Lincoln Laboratory 200-mm wafer fabrication platform for ultraviolet to near-IR wavelengths [13], which consists of a 100-nm-thick alumina (Al_2O_3) layer and two 100-nm-thick silicon-nitride (Si_3N_4) layers separated by 90 nm of silicon dioxide (SiO_2).

3.3.3 Adiabatic Polarization Rotator Design

First, we design an adiabatic polarization rotator which converts between the fundamental TE and TM modes on chip (Fig. 3.8a). This device begins with an asymmetric coupler that converts the input fundamental TE mode to the next higher order TE mode. The mode then enters an adiabatic taper, which passes through an anti-crossing between the higher order TE and fundamental TM modes, transferring power from one mode to the other. This anti-crossing is enabled by breaking the vertical symmetry via the dual SiN layer (Fig. 3.8a) [76]. By utilizing a three-stage taper that varies more rapidly on either side of the anti-crossing, the total device length is

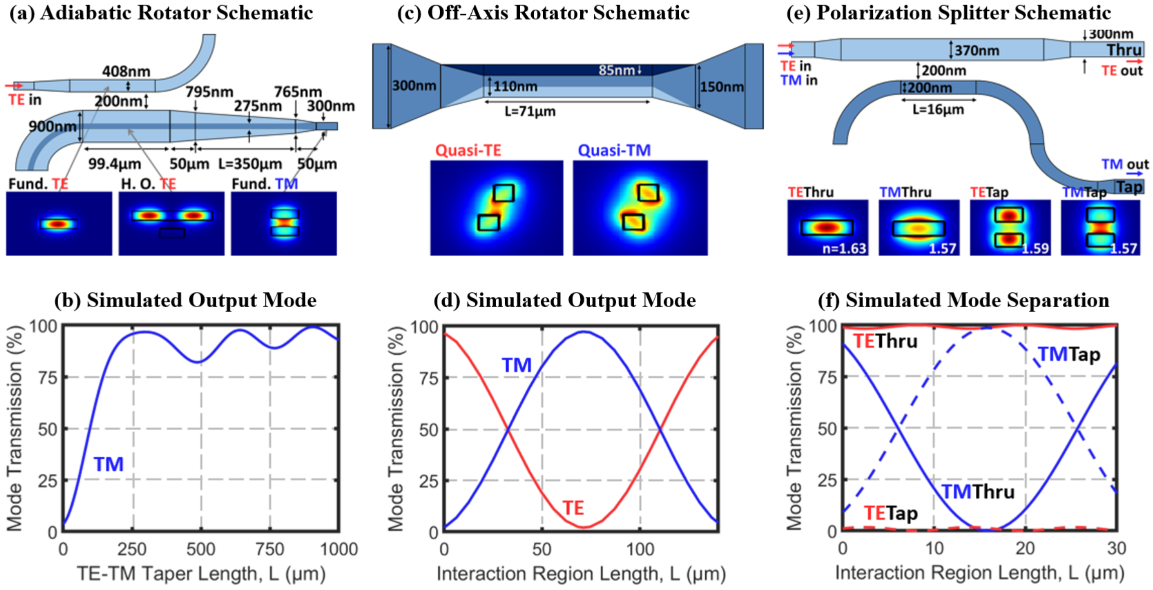

Figure 3.8: (a) Schematic (not to scale) of the adiabatic rotator, with relevant mode profiles shown. (b) Mode conversion efficiency of the adiabatic rotator as a function of TE-TM taper length. (c) Schematic of the off-axis rotator, with mode profiles that demonstrate the 45° optical axis rotation of the fundamental modes in the interaction region. (d) Mode conversion efficiency of the off-axis rotator as a function of interaction length. (e) Schematic of the polarization splitter, with mode profiles demonstrating the effective index match and contrast between the fundamental TM and TE modes, respectively. (f) Mode splitting efficiencies for the thru and tap ports for the polarization splitter as a function of interaction length.

reduced without a significant sacrifice in performance. The total device length is 550 µm, giving a simulated device efficiency of 93.78%, corresponding to an extinction ratio of 11.78 dB (Fig. 3.8b).

3.3.4 Off-Axis Polarization Rotator Design

As a complement to the above device, it is useful to have a more compact polarization rotator that can be used in more densely integrated systems. To this end, we also design an off-axis rotator that works on the principle of mode coupling between the two lowest-order modes (Fig. 3.8c), which have a high coupling coefficient [77]. By horizontally offsetting two stacked waveguides appropriately in the coupling region, both the fundamental modes become quasi-TE and TM, corresponding to an effective optical axis oriented at 45°. As a result, the fundamental modes exhibit beating and, by appropriate choice of length, the input TE mode can be efficiently converted to TM [77]. Gradual tapers into and out of the coupling region minimize radiative losses due to mode mismatch. The total device length is only 111 μm, achieving a simulated efficiency of 99.15%, corresponding to an extinction ratio of 20.7 dB (Fig. 3.8d).

3.3.5 Polarization Splitter Design

Third, we design an integrated asymmetric directional-coupler-based polarization splitter, using the dual SiN layers to maximize TM coupling into the tap port, while minimizing coupling of the TE mode (Fig. 3.8e). The device consists of a single-layer thru port and a dual-layer tap port, where the effective indices of the TM modes are matched between the two arms of the coupler. Due to their asymmetry, the two arms exhibit very different effective indices for TE [78] (Fig. 3.8e). As a result, the fundamental TM mode periodically strongly couples between the arms of the device along the length of the coupling region, while the TE mode exhibits only low-amplitude oscillations (Fig. 3.8f). The length of the coupling region of this device is only 16 μm, providing a compact device that allows for extinction ratios of 46.3 dB for TM input and 18.7 dB for TE input for their respective ports.

3.3.6 Conclusion

In this section, we designed the first integrated polarization rotators and splitter operating at blue wavelengths, enabling integrated polarization-diversity schemes, increased datacom channel density, and advanced chip-scale atomic systems.

Chapter 4

Optical Tweezing of Microspheres and Cells Using Integrated Optical Phased Arrays

The following work was led by Tal Sneh (MIT) and done in collaboration with Milica Notaros (MIT), Kru Kikkeri (MIT), Joel Voldman (MIT), and Jelena Notaros (MIT). This work has been published in [16, 17].

4.1 Introduction

Optical trapping and tweezing has garnered significant interest as a preferred technology for the non-contact manipulation of cells and microscale particles, producing impactful research for applications including cell classification, force sensing, and characterization [80, 81]. However, the cost, size, and complexity of these tools when using standard bulk-optical components has limited their utility. As an alternative, the development of on-chip optical traps has been pursued, using evanescent fields from waveguides, resonators, and plasmonic devices [82, 83]. While these systems have offered significant advantages in cost, form factor, and complexity, they have been restricted to trapping within microns of the chip surface, which limits their widespread adoption in practical biophysics experiments and for in-vivo applications that require millimeter-scale standoffs. In addition, many of these prior integrated optical tweezers have been fundamentally limited to passive trapping demonstrations that lack active spatial tuning of the optical fields, necessary for object tweezing and manipulation.

In contrast, integrated optical phased arrays (OPAs), which enable emission and non-mechanical control of arbitrary free-space radiation patterns from compact photonics chips, have the potential to resolve these limitations. Specifically, they provide a promising approach to extending the standoff operating distance, enabling spatial tuning for tweezing, and expanding to holographic multi-beam capability for sorting in the future. However, motivated by applications such as LiDAR sensing, the majority of integrated OPA demonstrations to date have been limited to generating and steering beams in the far field [44], which do not generate the tightly-focused beam profiles required for optical trapping. Recently, our group demonstrated the first integrated OPAs that enable these focusing beam profiles [12].

In this chapter, we demonstrate integrated OPA-based optical trapping and tweezing for the first time. The OPA system focuses the emitted light and provides a steerable potential-energy well that can be used to trap and tweeze microscale particles (Fig. 4.1a–b). Using this approach, we increase the standoff distance of integrated optical tweezers by over two orders of magnitude compared to prior demonstrations and show trapping and non-mechanical tweezing of polystyrene microspheres 5 mm above the surface of a silicon-photonic chip. We then use the tweezers to stretch mouse lymphoblast cells, showing, to the best of our knowledge, the first cell experiments using single-beam integrated optical tweezers.

4.2 Focusing Integrated Optical Phased Array Architecture

The near-field-focusing integrated OPA [12] was fabricated in a CMOS-compatible foundry process at the SUNY Polytechnic Institute. At the input, an inverse-taper

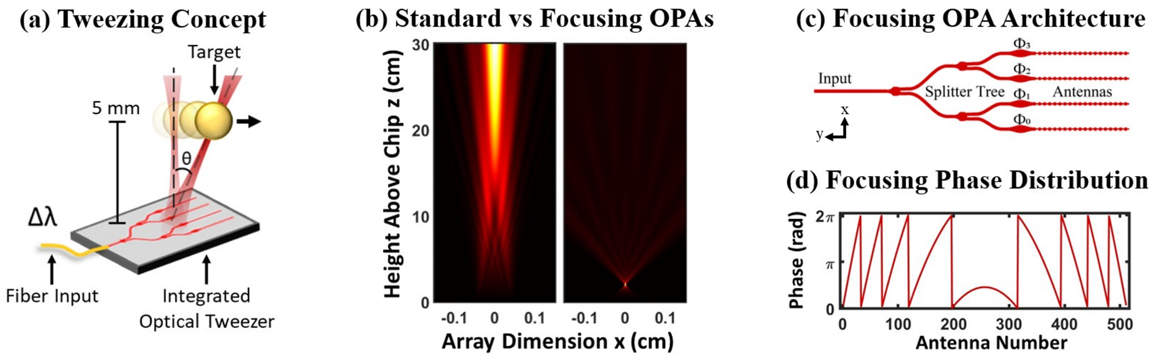
(a) Tweezing Concept
Target
5 mm
θ
Δλ
Fiber Input
Integrated Optical Tweezer
(b) Standard vs Focusing OPAs
Height Above Chip z (cm)
30
20
10
0
-0.1
0
0.1
-0.1
0
0.1
Array Dimension x (cm)
(c) Focusing OPA Architecture
Input
Splitter Tree
Antennas
Φ3
Φ2
Φ1
Φ0
x
y
(d) Focusing Phase Distribution
Phase (rad)
2π
π
0
100
200
300
400
500
Antenna Number

Figure 4.1: (a) Conceptual diagram depicting microsphere tweezing using an OPA by varying the input laser wavelength. (b) Simulated array-factor intensity above the chip for a standard non-focusing OPA (left) and near-field-focusing OPA with a 20-mm focal height (right). (c) Schematic of a passive splitter-tree-based focusing OPA architecture with 4 antennas (not to scale). (d) Element phase distribution for a focusing OPA with a 20-mm focal height, 512 antennas, 2-µm antenna pitch, and 1550-nm wavelength.

edge coupler couples light from a 1550-nm-wavelength off-chip tunable laser source into an on-chip silicon waveguide. A 9-stage splitter tree network then distributes the input power to 512 waveguide arms with a final pitch of 2 µm. Each arm is terminated with a 0.9-mm-long grating-based antenna that radiates the light upwards out of the chip. Before each antenna, a phase bump structure is placed to encode a static hyperbolic phase distribution (Fig. 4.1d) that enables focusing of the off-chip emission in the array dimension (x). Additionally, the antenna period is adiabatically chirped to enable focusing in the antenna dimension (y). The OPA architecture is shown in Fig. 4.1c. Additional details on the focusing integrated OPA are provided in [12].

4.3 Optical Trapping and Tweezing Results

To characterize our integrated OPA-based optical trap, the trap chip is mounted beneath a sample stage, and light is coupled onto the chip from a tunable benchtop laser.

To demonstrate optical trapping, we use samples consisting of two coverslips separated by a thickness of 375 µm, into which a 5.5% v/v solution of 10-µm-diameter polystyrene microspheres suspended in deionized water is pipetted. The sample is clamped into the stage, and a target sphere is moved into the focal spot of the trap, where its motion is recorded for 75 sec. To verify that the motion of the sphere is reduced specifically due to the trap, the laser is turned off, and the sphere's motion is recorded for an additional 75 sec. Using the TrackMate plugin for ImageJ [84], we track the motion of a group of microspheres, of which the middle sphere is trapped, as shown in Fig. 4.2a.

To quantify the trap's stiffness, we use the equipartition theorem and the mean squared displacement of spheres in the trap, measured using TrackMate [84, 85]. We perform four repeated measurements over a range of input powers. As shown in Fig. 4.2b, the results follow the expected linear trend, with error bars calculated as the standard error of the measurements.

To transform the system from a static trap to dynamic tweezers, we leverage the non-mechanical spot steering capability of our OPA system. Specifically, we vary the wavelength of the laser input into the OPA system to steer the location of the spot emitted by the OPA, resulting in the microsphere successfully following its motion. To demonstrate that the microsphere can be steered in arbitrary patterns in one dimension, we show repeated tweezing of the microsphere in a sine-wave pattern with two different frequencies (Fig. 4.2c–d).

Finally, we use the OPA system to perform, for the first time, cell experiments with single-beam integrated optical tweezers, showing controlled deformation of cells. We culture TIB-49 mouse lymphoblast cells in RPMI-1640 media with 10% Fetal Bovine Serum and 1% 10,000 U/mL Penicillin-Streptomycin. We incubate the cells at 37°C in a humidified 5% CO2 incubator and pipette them into a sample well. We position a cell in the optical trap and steer the trap in the y direction in the focal plane. We record the cell and observe that its bottom edge is attracted to the new trap position (Fig. 4.2e), leading to an increase in the cell aspect ratio of over 25% along its long axis. Upon turning off the laser, the cell relaxes to its prior unstretched state.

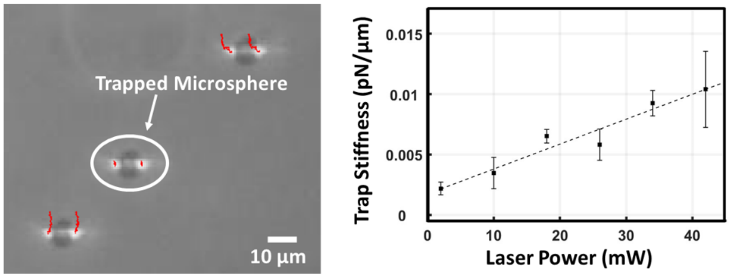

(a) Microsphere Trapping (b) Stiffness Characterization

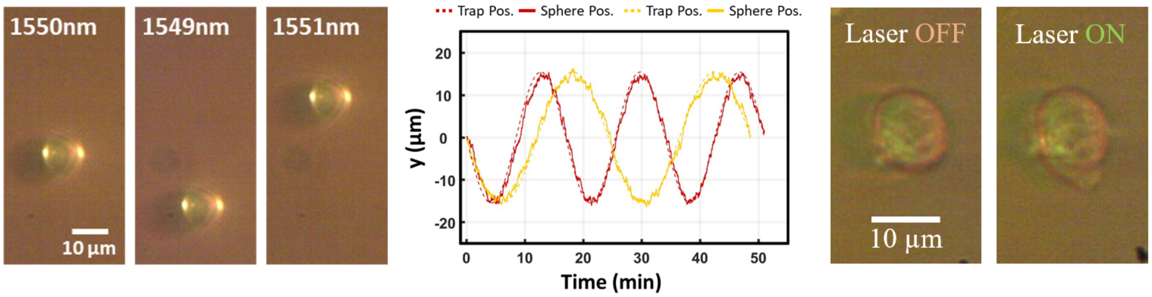

(c) Microsphere Tweezing (d) Periodic Tweezing (e) Cell Stretching

Figure 4.2: (a) Micrograph of microspheres in a sample well with superimposed tracks showing their motion over time (red lines); the motion of the microsphere located at the focal spot of the OPA (circled in white) is significantly reduced compared to its neighbors, indicating successful trapping. (b) Measured trap stiffness versus optical power for polystyrene microsphere trapping; error bars are found by calculating the standard error of the dataset. (c) Micrographs showing the position of a microsphere for input wavelengths of 1550nm (left), 1549nm (center), and 1551nm (right); the position varies with input wavelength, confirming successful tweezing. (d) Position of the spot formed by the optical trap (dashed line) and position of the optically tweezed microsphere (solid line) versus time for two different sinusoidal wavelength control signals, demonstrating consistent tweezing over arbitrary 1D patterns. (e) Micrograph showing a TIB-49 mouse lymphoblast cell trapped in the focus of the optical trap (left); the wavelength of the input laser is reduced by 0.6nm, steering the trap focus in the -y direction below the cell, resulting in the cell being stretched downward by the movement of the trap (right).

4.4 Conclusion

This chapter introduces a new modality for integrated optical tweezers, presenting a fundamentally different approach based on integrated OPAs that enables significantly larger standoff distances and arbitrary active tweezing functionality. This OPA-based approach offers the advantages in cost, footprint, complexity, and mass-producibility of integrated tweezers, while providing much of the functionality of bulk-optical systems. It thus represents a significant improvement in the utility and compatibility of integrated optical tweezers for biological research and opens the door to a variety of experiments that have not been previously possible with prior implementations of integrated tweezers, spanning biophysics research with microsphere-conjugated molecules, cell experimentation and sorting, and emerging in-vivo trapping research.

Chapter 5

Conclusion

In this thesis, we built upon recent advances in visible-light integrated photonics technologies to introduce 3D printing as a novel application area for visible-light integrated photonics [14], propose integrated-photonics-based system architectures for trapped-ion quantum systems [4] and demonstrate the design and testing of key devices for these architectures [15], and demonstrate integrated optical-phased-array-based optical trapping and tweezing for the first time [16, 17].

First, in Chapter 2, we combined the fields of silicon photonics and photochemistry to propose the first chip-based 3D printer. The proposed system consists of only a single millimeter-scale photonic chip without any moving parts that emits reconfigurable visible-light holograms up into a simple stationary resin well to enable non-mechanical volumetric 3D printing. Furthermore, we experimentally demonstrated a stereolithography-inspired proof-of-concept version of the chip-based 3D printer using a visible-light beam-steering integrated optical phased array and visible-light-curable resin, showing 3D printing using a chip-based system for the first time. This work demonstrates the first steps towards a highly-compact, portable, and low-cost solution for the next generation of 3D printers.

Second, in Chapter 3, we proposed integrated-photonics-based system architectures and the design of key integrated-photonics components for both polarization-gradient and electromagnetically-induced-transparency cooling of trapped ions. Specifically, we designed the systems for a wavelength of 422 nm to target the $S_{1/2}$ to $P_{1/2}$

transition of $^{88}\mathrm{Sr}^+$, a commonly used ion species for trapped-ion qubits. Further, we designed and experimentally demonstrated a pair of integrated TE- and TM-emitting gratings, representing the first development of integrated TM-emitting gratings for trapped-ion systems, and, thus, a fundamental stepping stone on the path to advanced operations for integrated-photonics-based trapped-ion quantum systems involving multiple polarizations. Then, we designed the first integrated polarization rotators and splitters operating at blue wavelengths.

Finally, in Chapter 4, we demonstrated integrated-optical-phased-array-based optical trapping and tweezing for the first time. The optical phased array system focuses emitted light and provides a steerable potential-energy well that can be used to trap and tweeze microscale particles. Using this approach, we increased the standoff distance of integrated optical tweezers by over two orders of magnitude compared to prior demonstrations and showed trapping and non-mechanical tweezing of polystyrene microspheres 5 mm above the surface of a silicon-photonic chip. We then used the tweezers to stretch mouse lymphoblast cells, showing, to the best of our knowledge, the first cell experiments using single-beam integrated optical tweezers.

Bibliography

[1] A. H. Atabaki, S. Moazeni, F. Pavanello, H. Gevorgyan, J. Notaros, L. Alloatti, M. T. Wade, C. Sun, S. A. Kruger, H. Meng, K. Al Qubaisi, I. Wang, B. Zhang, A. Khilo, C. V. Baiocco, M. A. Popović, V. M. Stojanović, and R. J. Ram, "Integrating photonics with silicon nanoelectronics for the next generation of systems on a chip," *Nature*, vol. 556, pp. 349–354, Apr. 2018.

[2] C. Sun, M. T. Wade, Y. Lee, J. S. Orcutt, L. Alloatti, M. S. Georgas, A. S. Waterman, J. M. Shainline, R. R. Avizienis, S. Lin, B. R. Moss, R. Kumar, F. Pavanello, A. H. Atabaki, H. M. Cook, A. J. Ou, J. C. Leu, Y.-H. Chen, K. Asanović, R. J. Ram, M. A. Popović, and V. M. Stojanović, "Single-chip microprocessor that communicates directly using light," *Nature*, vol. 528, pp. 534–538, Dec. 2015.

[3] R. J. Niffenegger, J. Stuart, C. Sorace-Agaskar, D. Kharas, S. Bramhavar, C. D. Bruzewicz, W. Loh, R. T. Maxson, R. McConnell, D. Reens, G. N. West, J. M. Sage, and J. Chiaverini, "Integrated multi-wavelength control of an ion qubit," *Nature*, vol. 586, pp. 538–542, Oct. 2020.

[4] A. Hattori, S. Corsetti, T. Sneh, M. Notaros, R. Swint, P. T. Callahan, C. D. Bruzewicz, F. Knollmann, R. McConnell, J. Chiaverini, and J. Notaros, "Integrated-photonics-based architectures for polarization-gradient and eit cooling of trapped ions," in *Frontiers in Optics + Laser Science 2022 (FIO, LS)*, p. FM4B.3, Optica Publishing Group, 2022.

[5] G. Moody, V. J. Sorger, D. J. Blumenthal, P. W. Juodawlkis, W. Loh, C. Sorace-Agaskar, A. E. Jones, K. C. Balram, J. C. F. Matthews, A. Laing, M. Davanco, L. Chang, J. E. Bowers, N. Quack, C. Galland, I. Aharonovich, M. A. Wolff, C. Schuck, N. Sinclair, M. Lončar, T. Komljenovic, D. Weld, S. Mookherjea1, S. Buckley, M. Radulaski1, S. Reitzenstein, B. Pingault, B. Machielse, D. Mukhopadhyay, A. Akimov, A. Zheltikov, G. S. Agarwal, K. Srinivasan, J. Lu, H. X. Tang, W. Jiang, T. P. McKenna, A. H. Safavi-Naeini, S. Steinhauer, A. W. Elshaari, V. Zwiller, P. S. Davids, N. Martinez, M. Gehl, J. Chiaverini, K. K. Mehta, J. Romero, N. B. Lingaraju, A. M. Weiner, D. Peace, R. Cernansky, M. Lobino, E. Diamanti, L. T. Vidarte, and R. M. Camacho, "2022 roadmap on integrated quantum photonics," *Journal of Physics: Photonics*, vol. 4, p. 012501, Oct. 2022.

[6] J. Wang, F. Sciarrino, A. Laing, and M. G. Thompson, "Integrated photonic quantum technologies," *Nature Photonics*, vol. 14, pp. 273–284, May 2020.

[7] D. T. Spencer, T. Drake, T. C. Briles, J. Stone, L. C. Sinclair, C. Fredrick, Q. Li, D. Westly, B. R. Ilic, A. Bluestone, N. Volet, T. Komljenovic, L. Chang, S. H. Lee, D. Y. Oh, M.-G. Suh, K. Y. Yang, M. H. P. Pfeiffer, T. J. Kippenberg, E. Norberg, L. Theogarajan, K. Vahala, N. R. Newbury, K. Srinivasan, J. E. Bowers, S. A. Diddams, and S. B. Papp, “An optical-frequency synthesizer using integrated photonics,” *Nature*, vol. 557, pp. 81–85, Apr. 2018.

[8] C. V. Poulton, M. J. Byrd, P. Russo, E. Timurdogan, M. Khandaker, D. Vermeulen, and M. R. Watts, “Long-range lidar and free-space data communication with high-performance optical phased arrays,” *IEEE J. Sel. Top. Quantum Electron.*, vol. 25, p. 7700108, 2019.

[9] J. Notaros, M. Notaros, M. Raval, C. V. Poulton, M. J. Byrd, N. Li, Z. Su, E. S. Magden, E. Timurdogan, T. Dyer, C. Baiocco, T. Kim, P. Bhargava, V. Stojanovic, and M. R. Watts, “Integrated optical phased arrays for lidar, communications, augmented reality, and beyond,” in *Applied Industrial Optics 2021*, p. M2A.3, Optica Publishing Group, 2021.

[10] J. Notaros, M. Raval, M. Notaros, and M. R. Watts, “Integrated-phased-array-based visible-light near-eye holographic projector,” in *Conference on Lasers and Electro-Optics*, p. STu3O.4, Optica Publishing Group, 2019.

[11] M. Notaros, T. Dyer, M. Raval, C. Baiocco, J. Notaros, and M. R. Watts, “Integrated visible-light liquid-crystal-based phase modulators,” *Optics Express*, vol. 30, no. 8, pp. 13790–13801, 2022.

[12] J. Notaros, C. V. Poulton, M. Raval, and M. R. Watts, “Near-field-focusing integrated optical phased arrays,” *Journal of Lightwave Technology*, vol. 36, no. 24, pp. 5912–5920, 2018.

[13] C. Sorace-Agaskar, D. Kharas, S. Yegnanarayanan, R. T. Maxson, G. N. West, W. Loh, S. Bramhavar, R. J. Ram, J. Chiaverini, J. Sage, and P. Juodawlkis, “Versatile silicon nitride and alumina integrated photonic platforms for the ultraviolet to short-wave infrared,” *IEEE Journal of Selected Topics in Quantum Electronics*, vol. 25, no. 5, pp. 1–15, 2019.

[14] S. Corsetti, M. Notaros, T. Sneh, A. Stafford, Z. A. Page, and J. Notaros, “Visible-light integrated optical phased arrays for chip-based 3d printing,” in *Optica Advanced Photonics Congress 2022*, p. IM2B.4, Optica Publishing Group, 2022.

[15] T. Sneh, A. Hattori, M. Notaros, S. Corsetti, and J. Notaros, “Design of integrated visible-light polarization rotators and splitters,” in *Frontiers in Optics + Laser Science 2022 (FIO, LS)*, p. JTu5A.48, Optica Publishing Group, 2022.

[16] T. Sneh, S. Corsetti, M. Notaros, and J. Notaros, “Focusing integrated optical phased arrays for chip-based optical trapping,” in *Conference on Lasers and Electro-Optics*, p. STh4G.4, Optica Publishing Group, 2022.

[17] T. Sneh, S. Corsetti, M. Notaros, K. Kikkeri, J. Voldman, and J. Notaros, "Optical tweezing of microspheres and cells using integrated optical phased arrays," in *2023 IEEE Photonics Conference (IPC)*, IEEE, 2023.

[18] B. Narupai and A. Nelson, "100th anniversary of macromolecular science viewpoint: Macromolecular materials for additive manufacturing," *ACS Macro Letters*, vol. 9, no. 5, pp. 627–638, 2020. PMID: 35648567.

[19] T. J. Wallin, J. Pikul, and R. F. Shepherd, "3D printing of soft robotic systems," *Nature Reviews Materials*, vol. 3, pp. 84–100, June 2018.

[20] S. C. Ligon, R. Liska, J. Stampfl, M. Gurr, and R. Mülhaupt, "Polymers for 3D printing and customized additive manufacturing," *Chem. Rev.*, vol. 117, pp. 10212–10290, Aug. 2017.

[21] R. L. Truby and J. A. Lewis, "Printing soft matter in three dimensions," *Nature*, vol. 540, pp. 371–378, Dec. 2016.

[22] Smart Bridge Amsterdam, "Mx3d bridge – a smart 3D-printed bridge." `https://www.smartbridgeamsterdam.com/`.

[23] A. Dobos, F. Gantner, M. Markovic, J. V. Hoorick, L. Tytgat, S. V. Vlierberghe, and A. Ovsianikov, "On-chip high-definition bioprinting of microvascular structures," *Biofabrication*, vol. 13, p. 015016, Dec. 2016.

[24] S. Sayer, T. Zandrini, M. Markovic, J. Van Hoorick, S. Van Vlierberghe, S. Baudis, W. Holnthoner, and A. Ovsianikov, "Guiding cell migration in 3D with high-resolution photografting," *Scientific Reports*, vol. 12, p. 8626, May 2022.

[25] H. J. McLennan, A. J. Blanch, S. J. Wallace, L. J. Ritter, S. L. Heinrich, D. K. Gardner, K. R. Dunning, M. J. Gauvin, A. K. Love, and J. G. Thompson, "Nanoliter perfusion microfluidic device made entirely by two-photon polymerization for dynamic cell culture with easy cell recovery," *Sci Rep*, vol. 13, p. 562, Jan. 2023.

[26] J. Hengsteler, B. Mandal, C. van Nisselroy, G. P. S. Lau, T. Schlotter, T. Zambelli, and D. Momotenko, "Bringing electrochemical Three-Dimensional printing to the nanoscale," *Nano Lett*, vol. 21, pp. 9093–9101, Oct. 2021.

[27] Relativity Space, "3D printed rockets." `https://www.relativityspace.com/`.

[28] N. Shahrubudin, T. Lee, and R. Ramlan, "An overview on 3d printing technology: Technological, materials, and applications," *Procedia Manufacturing*, vol. 35, pp. 1286–1296, 2019. The 2nd International Conference on Sustainable Materials Processing and Manufacturing, SMPM 2019, 8-10 March 2019, Sun City, South Africa.

[29] Formlabs, "Fdm vs. sla: compare filament and resin 3d printers." `https://formlabs.com/blog/fdm-vs-sla-compare-types-of-3d-printers/`, 2019.

[30] J. A. Lewis, "Direct ink writing of 3d functional materials," *Advanced Functional Materials*, vol. 16, no. 17, pp. 2193–2204, 2006.

[31] I. T. Ozbolat and M. Hospodiuk, "Current advances and future perspectives in extrusion-based bioprinting," *Biomaterials*, vol. 76, pp. 321–343, Oct. 2015.

[32] M. Schouten, G. Wolterink, A. Dijkshoorn, D. Kosmas, S. Stramigioli, and G. Krijnen, "A review of extrusion-based 3d printing for the fabrication of electro- and biomechanical sensors," *IEEE Sensors Journal*, vol. 21, pp. 12900–12912, 2021.

[33] A. Kafle, E. Luis, R. Silwal, H. M. Pan, P. L. Shrestha, and A. K. Bastola, "3D/4D printing of polymers: Fused deposition modelling (FDM), selective laser sintering (SLS), and stereolithography (SLA)," *Polymers (Basel)*, vol. 13, Sept. 2021.

[34] F. P. W. Melchels, J. Feijen, and D. W. Grijpma, "A review on stereolithography and its applications in biomedical engineering," *Biomaterials*, vol. 31, pp. 6121–6130, May 2010.

[35] A. Sullivan, "Depthcube solid-state 3d volumetric display," in *SPIE 5291, Stereoscopic Displays and Virtual Reality Systems XI*, SPIE, 2004.

[36] B. E. Kelly, I. Bhattacharya, H. Heidari, M. Shusteff, C. M. Spadaccini, and H. K. Taylor, "Volumetric additive manufacturing via tomographic reconstruction," *Science*, vol. 363, pp. 1075–1079, Jan. 2019.

[37] M. Regehly, Y. Garmshausen, M. Reuter, N. F. König, E. Israel, D. P. Kelly, C.-Y. Chou, K. Koch, B. Asfari, and S. Hecht, "Xolography for linear volumetric 3d printing," *Nature*, vol. 588, pp. 620 – 624, 2020.

[38] M. Shusteff, A. E. M. Browar, B. E. Kelly, J. Henriksson, T. H. Weisgraber, R. M. Panas, N. X. Fang, and C. M. Spadaccini, "One-step volumetric additive manufacturing of complex polymer structures," *Science Advances*, vol. 3, no. 12, p. eaao5496, 2017.

[39] P. Bhargava, T. Kim, C. V. Poulton, J. Notaros, A. Yaacobi, E. Timurdogan, C. Baiocco, N. Fahrenkopf, S. Kruger, T. Ngai, Y. Timalsina, M. R. Watts, and V. Stojanović, "Fully integrated coherent lidar in 3d-integrated silicon photonics/65nm cmos," in *2019 Symposium on VLSI Circuits*, pp. C262–C263, 2019.

[40] C. V. Poulton, A. Yaacobi, D. B. Cole, M. J. Byrd, M. Raval, D. Vermeulen, and M. R. Watts, "Coherent solid-state lidar with silicon photonic optical phased arrays," *Opt. Lett.*, vol. 42, pp. 4091–4094, Oct 2017.

[41] J. Sun, E. Timurdogan, A. Yaacobi, E. S. Hosseini, and M. R. Watts, "Large-scale nanophotonic phased array," *Nature*, vol. 493, pp. 195–199, Jan. 2013.

[42] T. Kim, P. Bhargava, C. Poulton, J. Notaros, A. Yaacobi, E. Timurdogan, C. Baiocco, N. Fahrenkopf, S. Kruger, T. Ngai, Y. Timalsina, M. Watts, and V. Stojanovic, "A single-chip optical phased array in a wafer-scale silicon photonics / cmos 3d-integration platform," *IEEE Journal of Solid-State Circuits*, vol. PP, pp. 1–14, 09 2019.

[43] J. Notaros, C. V. Poulton, M. Raval, and M. R. Watts, "Near-field-focusing integrated optical phased arrays," *Journal of Lightwave Technology*, vol. 36, no. 24, pp. 5912–5920, 2018.

[44] J. Notaros, N. Li, C. V. Poulton, Z. Su, M. J. Byrd, E. S. Magden, E. Timurdogan, C. Baiocco, N. M. Fahrenkopf, and M. R. Watts, "Cmos-compatible optical phased array powered by a monolithically-integrated erbium laser," *J. Lightwave Technol.*, vol. 37, pp. 5982–5987, Dec 2019.

[45] M. J. Heck, "Highly integrated optical phased arrays: photonic integrated circuits for optical beam shaping and beam steering," *Nanophotonics*, vol. 6, no. 1, pp. 93–107, 2017.

[46] T. Komljenovic, R. Helkey, L. Coldren, and J. E. Bowers, "Sparse aperiodic arrays for optical beam forming and lidar," *Opt. Express*, vol. 25, pp. 2511–2528, Feb 2017.

[47] F. Aflatouni, B. Abiri, A. Rekhi, and A. Hajimiri, "Nanophotonic projection system," *Opt. Express*, vol. 23, pp. 21012–21022, Aug 2015.

[48] R. Fatemi, A. Khachaturian, and A. Hajimiri, "A nonuniform sparse 2-d large-fov optical phased array with a low-power pwm drive," *IEEE Journal of Solid-State Circuits*, vol. 54, no. 5, pp. 1200–1215, 2019.

[49] D. Hutchison, J. Sun, J. Doylend, R. Kumar, J. Heck, W. Kim, C. Phare, A. Feshali, and H. Rong, "High-resolution aliasing-free optical beam steering," *Optica*, vol. 3, p. 887, 08 2016.

[50] J. Notaros, C. V. Poulton, M. J. Byrd, M. Raval, and M. R. Watts, "Integrated optical phased arrays for quasi-bessel-beam generation," *Opt. Lett.*, vol. 42, pp. 3510–3513, Sep 2017.

[51] J. Zhou, J. Sun, A. Yaacobi, C. Poulton, and M. Watts, "Design of 3d hologram emitting optical phased arrays," *Integrated Photonics Research, Silicon and Nanophotonics, IPRSN 2015*, 01 2015.

[52] A. Bagheri and J. Jin, "Photopolymerization in 3D printing," *ACS Appl. Polym. Mater.*, vol. 1, pp. 593–611, Apr. 2019.

[53] D. Ahn, L. M. Stevens, K. Zhou, and Z. A. Page, "Rapid High-Resolution visible light 3D printing," *ACS Cent Sci*, vol. 6, pp. 1555–1563, Aug. 2020.

[54] A. Stafford, D. Ahn, E. K. Raulerson, K.-Y. Chung, K. Sun, D. M. Cadena, E. M. Forrister, S. R. Yost, S. T. Roberts, and Z. A. Page, "Catalyst halogenation enables rapid and efficient polymerizations with visible to Far-Red light," *J. Am. Chem. Soc.*, vol. 142, pp. 14733–14742, Aug. 2020.

[55] J. W. Goodman, *Introduction to Fourier Optics*. McGraw-Hill, 1996.

[56] M. S. Hai, A. Leinse, T. Veenstra, and O. Liboiron-Ladouceur, "A thermally tunable 1 × 4 channel wavelength demultiplexer designed on a low-loss si3n4 waveguide platform," *Photonics*, vol. 2, no. 4, pp. 1065–1080, 2015.

[57] Z. Yong, H. Chen, X. Luo, A. Govdeli, H. Chua, S. S. Azadeh, A. Stalmashonak, G.-Q. Lo, J. K. S. Poon, and W. D. Sacher, "Power-efficient silicon nitride thermo-optic phase shifters for visible light," *Opt. Express*, vol. 30, pp. 7225–7237, Feb 2022.

[58] M. Notaros, T. Dyer, M. Raval, C. Baiocco, J. Notaros, and M. R. Watts, "Integrated visible-light liquid-crystal-based phase modulators," *Opt. Express*, vol. 30, pp. 13790–13801, Apr 2022.

[59] J. Notaros, M. Notaros, M. Raval, and M. R. Watts, "Liquid-crystal-based visible-light integrated optical phased arrays," in *Conference on Lasers and Electro-Optics*, p. STu3O.3, Optica Publishing Group, 2019.

[60] A. Garcia Coleto, M. Notaros, and J. Notaros, "Integrated liquid-crystal-based modulators: packaging processes and evaluation techniques," in *2023 IEEE Photonics Conference (IPC)*, IEEE, 2023.

[61] P. Garra, C. Dietlin, F. Morlet-Savary, F. Dumur, D. Gigmes, J.-P. Fouassier, and J. Lalevée, "Redox two-component initiated free radical and cationic polymerizations: Concepts, reactions and applications," *Progress in Polymer Science*, vol. 94, pp. 33–56, 2019.

[62] E. Blasco, M. Wegener, and C. Barner-Kowollik, "Photochemically driven polymeric network formation: Synthesis and applications," *Advanced Materials*, vol. 29, no. 15, p. 1604005, 2017.

[63] J. K. Matsui, S. B. Lang, D. R. Heitz, and G. A. Molander, "Photoredox-Mediated routes to radicals: The value of catalytic radical generation in synthetic methods development," *ACS Catal.*, vol. 7, pp. 2563–2575, Apr. 2017.

[64] S. Dadashi-Silab, S. Doran, and Y. Yagci, "Photoinduced electron transfer reactions for macromolecular syntheses," *Chem. Rev.*, vol. 116, pp. 10212–10275, Sept. 2016.

[65] M. Chen, M. Zhong, and J. A. Johnson, "Light-Controlled radical polymerization: Mechanisms, methods, and applications," *Chem. Rev.*, vol. 116, pp. 10167–10211, Sept. 2016.

[66] J. C. Koziar and D. O. Cowan, "Photochemical heavy-atom effects.," *Acc. Chem. Res.*, vol. 11, pp. 334–341, 1978.

[67] C. D. Bruzewicz, J. Chiaverini, R. McConnell, and J. M. Sage, "Trapped-ion quantum computing: Progress and challenges," *Applied Physics Reviews*, vol. 6, no. 2, p. 021314, 2019.

[68] K. K. Mehta, C. Zhang, M. Malinowski, T.-L. Nguyen, M. Stadler, and J. P. Home, "Integrated optical multi-ion quantum logic," *Nature*, vol. 586, pp. 533–537, Oct. 2020.

[69] M. Joshi, A. Fabre, C. Maier, T. Brydges, D. Kiesenhofer, H. Hainzer, R. Blatt, and C. Roos, "Polarization-gradient cooling of 1d and 2d ion coulomb crystals," *New Journal of Physics*, vol. 22, p. 103013, 10 2020.

[70] C. F. Roos, D. Leibfried, A. Mundt, F. Schmidt-Kaler, J. Eschner, and R. Blatt, "Experimental demonstration of ground state laser cooling with electromagnetically induced transparency," *Phys. Rev. Lett.*, vol. 85, pp. 5547–5550, Dec 2000.

[71] L. Massai, T. Schatteburg, J. P. Home, and K. K. Mehta, "Pure circularly polarized light emission from waveguide microring resonators," *Applied Physics Letters*, vol. 121, p. 121101, 09 2022.

[72] G. Spektor, D. Carlson, Z. Newman, J. L. Skarda, N. Sapra, L. Su, S. Jammi, A. R. Ferdinand, A. Agrawal, J. Vučković, and S. B. Papp, "Universal visible emitters in nanoscale integrated photonics," *Optica*, vol. 10, pp. 871–879, Jul 2023.

[73] J. Notaros, F. Pavanello, M. T. Wade, C. M. Gentry, A. Atabaki, L. Alloatti, R. J. Ram, and M. A. Popović, "Ultra-efficient cmos fiber-to-chip grating couplers," in *Optical Fiber Communication Conference*, p. M2I.5, Optica Publishing Group, 2016.

[74] C. Sun, Y. Yu, Y. Ding, Z. Li, W. Qi, and X. Zhang, "Integrated mode-transparent polarization beam splitter supporting thirteen data channels," *Photon. Res.*, vol. 8, pp. 978–985, Jun 2020.

[75] M. R. Watts and H. A. Haus, "Integrated mode-evolution-based polarization rotators," *Opt. Lett.*, vol. 30, pp. 138–140, Jan 2005.

[76] D. Dai and J. E. Bowers, "Novel concept for ultracompact polarization splitter-rotator based on silicon nanowires," *Opt. Express*, vol. 19, pp. 10940–10949, May 2011.

[77] Z. Wang and D. Dai, "Ultrasmall si-nanowire-based polarization rotator," *J. Opt. Soc. Am. B*, vol. 25, pp. 747–753, May 2008.

[78] F. Zhang, J. Zheng, Y. Song, W. Liu, P. Xu, and A. Majumdar, "Ultra-broadband and compact polarizing beam splitter in silicon photonics," *OSA Continuum*, vol. 3, pp. 560–567, Mar 2020.

[79] K. Gallacher, P. Griffin, E. Riis, M. Sorel, and D. Paul, "Silicon nitride waveguide polarization rotator and polarization beam splitter for chip-scale atomic systems," *APL Photonics*, vol. 7, p. 046101, 04 2022.

[80] A. Ashkin, "Acceleration and trapping of particles by radiation pressure," *Phys. Rev. Lett.*, vol. 24, pp. 156–159, Jan 1970.

[81] O. M. Marago, P. Jones, P. Gucciardi, G. Volpe, and A. Ferrari, "Optical trapping and manipulation of nanostructures," *Nature nanotechnology*, vol. 8, pp. 807–19, 11 2013.

[82] M. Juan, M. Righini, and R. Quidant, "Plasmon nano-optical tweezers," *Nature Photonics*, vol. 5, p. 349, 05 2011.

[83] Y. Sun, X.-C. Yuan, L. Ong, J. Bu, S. Zhu, and R. Liu, "Large-scale optical traps on a chip for optical sorting," *Applied Physics Letters*, vol. 90, pp. 031107–031107, 01 2007.

[84] J.-Y. Tinevez, N. Perry, J. Schindelin, G. M. Hoopes, G. D. Reynolds, E. Laplantine, S. Y. Bednarek, S. L. Shorte, and K. W. Eliceiri, "Trackmate: An open and extensible platform for single-particle tracking," *Methods*, vol. 115, pp. 80–90, 2017. Image Processing for Biologists.

[85] G. Pesce, G. Volpe, O. M. Marago, P. Jones, S. Gigain, A. Sasso, and G. Volpe, "A step-by-step guide to the realisation of advanced optical tweezers," *Journal of the Optical Society of America B*, vol. 32, pp. B84–B98, 04 2015.